SANDIA REPORT
SAND2015-8066
Unlimited Release
September 2015

A Process and Environment Aware Sierra/SolidMechanics Cohesive Zone Modeling Capability for Polymer/Solid Interfaces

E. D. Reedy, Jr.
R. S. Chambers
Component Science & Mechanics

L. G. Hughes
J. M. Kropka
M. E. Stavig
Organic Materials Science

M. J. Stevens
Computational Materials & Data Science

Prepared by
Sandia National Laboratories
Albuquerque, New Mexico 87185 and Livermore, California 94550

Sandia National Laboratories is a multi-program laboratory managed and operated by Sandia Corporation,
a wholly owned subsidiary of Lockheed Martin Corporation, for the U.S. Department of Energy's
National Nuclear Security Administration under contract DE-AC04-94AL85000.

Sandia National Laboratories

Issued by Sandia National Laboratories, operated for the United States Department of Energy by Sandia Corporation.

Printed in the United States of America. This report has been reproduced directly from the best available copy.

Available to DOE and DOE contractors from
U.S. Department of Energy
Office of Scientific and Technical Information
P.O. Box 62
Oak Ridge, TN 37831

Telephone: (865) 576-8401
Facsimile: (865) 576-5728
E-Mail: reports@osti.gov
Online ordering: http://www.osti.gov/scitech

Available to the public from
U.S. Department of Commerce
National Technical Information Service
5301 Shawnee Rd
Alexandria, VA 22312

Telephone: (800) 553-6847
Facsimile: (703) 605-6900
E-Mail: orders@ntis.gov
Online order: http://www.ntis.gov/search

SAND2015-8066
Unlimited Release
September 2015

A Process and Environment Aware Sierra/SolidMechanics Cohesive Zone Modeling Capability for Polymer/Solid Interfaces

E. D. Reedy, Jr.
R. S. Chambers
Component Science & Mechanics

L. G. Hughes
J. M. Kropka
M. E. Stavig
Organic Materials Science

M. J. Stevens
Computational Materials & Data Science

Sandia National Laboratories
P.O. Box 5800
Albuquerque, New Mexico 87185-MS0889

Abstract

The performance and reliability of many mechanical and electrical components depend on the integrity of polymer-to-solid interfaces. Such interfaces are found in adhesively bonded joints, encapsulated or underfilled electronic modules, protective coatings, and laminates. The work described herein was aimed at improving Sandia's finite element –based capability to predict interfacial crack growth by 1) using a high fidelity nonlinear viscoelastic material model for the adhesive in fracture simulations, and 2) developing and implementing a novel cohesive zone fracture model that generates a mode-mixity dependent toughness as a natural consequence of its formulation (i.e., generates the observed increase in interfacial toughness with increasing crack-tip interfacial shear). Furthermore, molecular dynamics simulations were used to study fundamental material/interfacial physics so as to develop a fuller understanding of the connection between molecular structure and failure. Also reported are test results that quantify how joint strength and interfacial toughness vary with temperature.

ACKNOWLEDGMENTS

This work was supported by the Laboratory Directed Research and Development program at Sandia National Laboratories. Sandia National Laboratories is a multi-program laboratory managed and operated by Sandia Corporation, a wholly owned subsidiary of Lockheed Martin Corporation, for the U.S. Department of Energy's National Nuclear Security Administration under contract DE-AC04-94AL85000.

CONTENTS

FIGURES

TABLES

1. INTRODUCTION

The goal of this work was to develop an improved finite element-based simulation capability to predict the performance and reliability of polymer-to-solid interfaces. This work was motivated by the fact that interfacial failure can severely impact a component's structural integrity and its ability to resist electrical breakdown. The integrity of a polymer/solid interface depends on the polymer and its cure cycle, surface preparation, and the thermal-mechanical loading history. Component geometry and materials also influence the mix of shear-to-normal interfacial stress that is generated by residual and applied loads and as such have an effect on how the interface separates. An interface designed to resist interfacial shear is not necessarily optimized to resist interfacial tension.

This report begins by presenting experimental results that demonstrate how joint strength and interfacial toughness vary with temperature (Section 2). In general the epoxy bond in such specimens contains residual stress that is introduced during the processing step. The residua stress will depend on the polymer's constitutive response, which in turn depends on cure schedule and the thermo-mechanical history to which the polymer is subjected. For this reason, we used a nonlinear viscoelastic (NLVE) polymer constitutive model to capture the highly nonlinear relaxations that can occur during processing, aging, and thermo-mechanical loading. This particular model (the Simplified Potential Energy Clock or NLVE SPEC model) is physically based and can predict the full range of polymer behavior, including stress/volume relaxation, physical aging and yielding (Adolf, Chambers et al., 2004). Section 3 of this report describes the SPEC nonlinear viscoelastic constitutive model and the type of experimental data that is needed to calibrate the model. Section 3 also presents the underlying data and material parameter choices for the epoxy models used in the calculations reported herein. This is also the same epoxy as used in the tests described in Section 2.

Section 4 of the report presents results of a detailed nonlinear viscoelastic analysis of a tensile loaded, adhesively bonded, rigid adherend butt joint (i.e., used the NLVE SPEC model). This is a prototypical crack initiation problem and there is no pre-existing crack in this plane strain analysis. Nonetheless, interfacial normal and shear stress exhibit a steep stress gradient as the stress-free edge is approached. Indeed, within the context of elasticity theory the stress is singular at the interface corner (where the interface meets the stress-free edge). The NLVE SPEC analysis results are compared to linear elastic results so as to estimate the size of the region dominated by nonlinear response.

Section 5 describes a conceptually simple cohesive zone model that generates a mode-mixity dependent toughness (i.e., generates the observed increase in interfacial toughness with increasing crack-tip interfacial shear). This Mode-mixity Dependent Toughness Cohesive Zone Model (MDG$_c$ CZM) was developed during the course of this project (Reedy and Emery 2014). The nature of predictions made by analyses that use the MDG$_c$ CZM is illustrated by considering the classic problem an edge-cracked elastic layer that is sandwiched between rigid adherends. This geometry is similar to that which has been used to measure the dependence of interfacial toughness on crack-tip mode-mixity and calculated results are compared to published data.

Section 6 present results of calculations that use the NLVE SPEC for the adhesive constitutive model and the MDG$_c$ CZM for interfacial separation. Note that both the NLVE SPEC constitutive model and the MDG$_c$ CZM are implemented in the production version of Sierra/SM. The NLVE SPEC model is used to account for yield-like behavior and residual stress outside of the immediate region of the fracture process zone while the MDGc CZM models the fracture process zone. A tensile-loaded, adhesively bonded, rigid adherend butt joint with an interfacial edge flaw is analyzed. The joint is loaded by first applying a uniform temperature change that induces residual stress within the bond and then applying a tensile load. Results for an initial short crack are contrasted with those for a long crack. The results are also compared to results of a linear elastic fracture mechanics analysis. The inclusion of residual stress is important since the magnitude of residual stress in high glass transition temperature glassy polymers can be significant (10's of MPa).

Section 7, the final major section of this report, presents molecular dynamics (MD) results for a rigid-adherend, adhesively bonded butt joint. These calculations used a new coarse-grained model for highly crosslinked polymer networks to more accurately represent molecular packing at the interface and bond failure. The simulations focused on how system size affects fracture initiation and crack growth.

2. FRACTURE TESTS

2.1 Tensile-loaded, adhesively bonded cylindrical butt joint

The adhesively bonded butt joints were formed by bonding two 6061-T6 aluminum rods together with an epoxy adhesive. The adherends are solid cylinders (28.6 mm diameter by 38.1 mm long) that have been precision machined to guarantee that the ends are flat and perpendicular to the cylinder axis (the edges were left sharp). The bonding surfaces of the aluminum adherends were lightly grit blasted (60 grit alumina oxide at 50 psi). The surfaces were cleaned by sonicating in deionized water for 10 minutes, immediately removing and wiping clean with isopropyl alcohol, wiping again with isopropyl alcohol, and finally drying with nitrogen. Each joint was assembled in a V-block fixture to ensure alignment of the two adherends, and a room temperature vulcanization (RTV) silicone (RTV 630, Momentive) boot was used to hold the epoxy resin in the bond gap during cure. The adherends were clamped to the alignment fixture during the filling operation to prevent motion. Clamps were removed prior to curing, such that the silicone boot was the only constraint to adherend axial motion. The silicone boot contained an injection hole and a reservoir to accommodate epoxy shrinkage. The epoxy adhesive is a diglycidyl ether of bisphenol A (EPON® Resin 828, Hexion) cured with Jeffamine® T-403 polyetheramine (Huntsman) at 43 parts per hundred resin. The adhesive was cured according to the following schedule: 24 hr. at 23^{o}C, followed by 3 hr. at 50^{o}C, followed by 15 hr. at 80^{o}C. After cure, the joints were annealed at 110^{o}C for 15 min. to erase the processing history and then cooled to 23^{o}C at 2^{o}C/min. to define a known thermal history of the structure prior to testing. The adhesive exhibits a glass transition that exhibits a midpoint at 85^{o}C when measured by thermal mechanical analysis. Compression tests of strain-gauged, molded epoxy plugs cured in the same manner and tested at room temperature (RT) and at a strain rate of 0.0001/s were used to measure the epoxy's elastic properties. The measured Young's modulus E equals 3.15 GPa while the Poisson's ratio ν equals 0.39. The epoxy's measured RT compressive yield strength at a strain rate of ~0.0003/s is 80 MPa.

Table 2-1 reports the results for two sets of nominally identical butt joints (referred to as set 1 and set 2), where the target bond thickness h was one mm. Each set of joints was split into two groups, with one half of the joints tested at room temperature and the other half tested at -50^{o}C. For a given test temperature, the average strength of set 1 and 2 joints is quite consistent, suggesting good reproducibility in the fabrication procedures. Interestingly, the tensile strength of the joints increased by 40% as test temperature was lowered from RT to -50^{o}C even though one might expect the epoxy to be more brittle and the residual stress to be higher at the lower temperature.

2.2 Asymmetric Double Cantilevered Beam Sandwich Specimen

The Asymmetric Double Cantilevered Beam Sandwich (ADCBS) specimen was used to measure interfacial toughness. Interfacial toughness is a material property that characterizes the energy to propagate an existing interfacial crack. One aspect of interfacial fracture mechanics that distinguishes it from traditional linear elastic fracture mechanics is the role of crack-tip mode-mixity (Rice 1988; Hutchinson and Suo 1992). Asymmetries with respect to the interface are responsible for the inherently mixed-mode condition found at the tip of an interfacial crack. Even for a symmetric loading, elastic asymmetry generates both normal and shear stress on the interface ahead of the crack tip and the ratio of these stresses changes with distance from the crack tip. The level of mode-mixity $\psi_{r=l}$ (defined as the arctangent of the ratio of the shear stress to normal stress at a fixed distance *l* in front of the crack tip in the region dominated by the stress singularity) depends on the mismatch in elastic properties as well as specimen geometry and loading. Mode-mixity is important because the value of the interfacial toughness depends on the level of mode-mixity. The ADCBS specimen used in this study bonds 4.7 and 8.9 mm thick 6061-T6 aluminum beams together with a thin epoxy layer (both beams are 12.8 mm deep and 120 mm long). This specimen produces a predominantly Mode I-like loading near the crack-tip with a slight tendency to push the crack towards and keep it on the interface. The specimen is pinned into a load train that utilizes a chain linkage and is loaded by pulling the ends apart at a crosshead displacement rate of 0.02 mm/s to propagate a crack along the interface with the thinner beam. The crack grows stably with increasing end displacement allowing several toughness measurements to be made while testing a single specimen. Crack length is inferred from specimen compliance, and the specimen is unloaded and reloaded several times during the test to establish the crack length during the loading step. The calibration used to determine toughness values from the inferred crack length and the load at the initiation of crack growth is based on published results for a homogeneous asymmetrical double cantilever beam specimen that ignores the compliance of the thin adhesive bond (Bao, Ho et al. 1992). These results for a homogeneous specimen can be converted to those applicable to a sandwich test specimen with a middle layer that is thin relative to other dimensions (Suo and Hutchinson 1989). Using this conversion, the sandwich specimen employed in this study has a crack-tip mode-mixity $\psi_{r=0.01\ \mathrm{mm}}$ of about -20^o.

The same surface preparation as used for the butt joints was used for the ADCBS specimens (see the previous section). The measured root mean square surface roughness R_q was 4 μm. Small spacers are bonded to the ends of one of the adherends to define the epoxy layer thickness and the edges of the specimen are sealed with Teflon tape to form a cavity that is to be filled with epoxy. The cavity is filled by injecting epoxy through a small hole in one end of the thicker beam and allowing the epoxy to flow along the entire length of the cavity and then out of a small hole on the opposing end of the beam.

Table 2-2 presents ADCBS data that quantifies the dependence of interfacial toughness on test temperature, epoxy cure cycle, and bond thickness. Set 1 samples have a 1.1 mm-thick bond while Set 2 samples have a 0.5 mm-thick bond. All Set 1 samples were cured for 24 hr. at 23^{o}C, followed by 3 hr. 50^{o}C, followed by 15 hr at 80^{o}C. One of these samples was also annealed at 110^{o}C for 15 min and cooled to 23^{o}C at 2^{o}C/min prior to testing. Half of Set 2 samples were cured in the same way as Set 1 samples (and all of these samples were subjected to the annealing step prior to testing). The other half of the Set 2 samples were cured using an alternate curing schedule that had been used in previous studies (Reedy and Guess 1999). These samples were cured for 24 hr. at 23^{o}C, followed by 24 hr. at 50^{o}C, followed by 24 hr. 40^{o}C). Test temperature had the most striking effect. The interfacial toughness increased by 85% as the test temperature decreased from room temperature to -65^{o}C (Fig. 2-1, averaged Table 2-2 toughness at each test temperature). On the other hand, there was no significant change in toughness when the bond thickness was decreased from 1.1 mm to 0.5 mm. Likewise; the samples fabricated using either of the cure cycles had similar measured toughness.

Table 2-3 presents additional ADCBS data that quantifies the dependence of interfacial toughness on surface roughness and the presence of a gold coating (set 3 samples). As anticipated, both surface roughness and the presence of a gold coating have a strong impact on the measured interfacial toughness. Reducing the surface roughness from an estimated R_q of 4 μm (grit blasted) to an estimated R_q of 0.1 μm (polished surface) decreased the measured interfacial toughness by almost a factor of ten. Note that set 2 sample 2 is nominally identical to set 3 samples 1-3, although the set 3 samples have a significantly higher toughness (~118 J/m^2 vs. ~87 J/m^2). This is presumably associated with uncontrolled variations in the fabrication process and suggests the need for additional study (e.g., perhaps due to slightly different surface roughness or other factors that influence surface cleanliness, etc.).

Table 2-1. Butt joint strength data.

set	h (mm)	test temp. (^{o}C)	# tested	avg. σ_f (MPa)	st. dev. σ_f (MPa)
1	1.05	23	5	27.4	1.8
1	1.10	-50	5	37.8	5.1
2	0.97	23	10	26.9	3.6
2	1.01	-50	9	38.1	2.5

Table 2-2. Interfacial toughness vs. test temperature and cure cycle (all specimens with a grit blasted surface).

set	sample	h (mm)	test temp. (°C)	cure[1]	# data points	avg. Γ (J/m^2)	st. dev. Γ (J/m^2)
1	1	1.1	RT	1-no anneal	3	87	4
1	2	1.1	-25	1-no anneal	5	129	4
1	3	1.1	-65	1-no anneal	3	159	3
1	4	1.1	-65	1- annealed	5	154	5
2	1	0.5	RT	1- annealed	5	92	4
2	2	0.5	RT	2	5	87	3
2	3	0.5	-25	1- annealed	5	124	4
2	4	0.5	-25	2	5	121	2
2	5	0.5	-65	1- annealed	4	169	3
2	6	0.5	-65	2	4	162	3

[1] cure 1: 24 hr. at 23°C, followed by 3 hr. 50°C, followed by 15 hr. at 80°C. If annealed, annealed at 110°C for 15 min. and cooled to 23°C at 2°C/min. prior to test).

cure 2: 24 hr. at 23°C, 24 hr. at 50°C, followed by 24 hr. 40°C

Table 2-3. Interfacial toughness vs. surface roughness or presence of a gold coating (all tests at RT with specimens fabricated using cure 11 and with a 0.5 mm bond).

set	sample	surface roughness	surface coating	# data points	avg. Γ (J/m^2)	st. dev. Γ (J/m^2)
3	1	grit-blasted	none	5	118	6
3	2	grit-blasted	none	5	119	4
3	3	grit-blasted	none	5	116	11
3	4	grit-blasted	gold	5	68	4
3	5	grit-blasted	gold	4	66	4
3	6	grit-blasted	gold	5	66	3
3	7	polished	none	3	14	0.4
3	8	polished	none	5	14	1.1
3	9	polished	none	5	13	0.7

[1] cure 1: 24 hr. at 23°C, followed by 3 hr. 50°C, followed by 15 hr. at 80°C. Annealed at 110°C for 15 min. and cooled to 23°C at 2°C/min. prior to test.

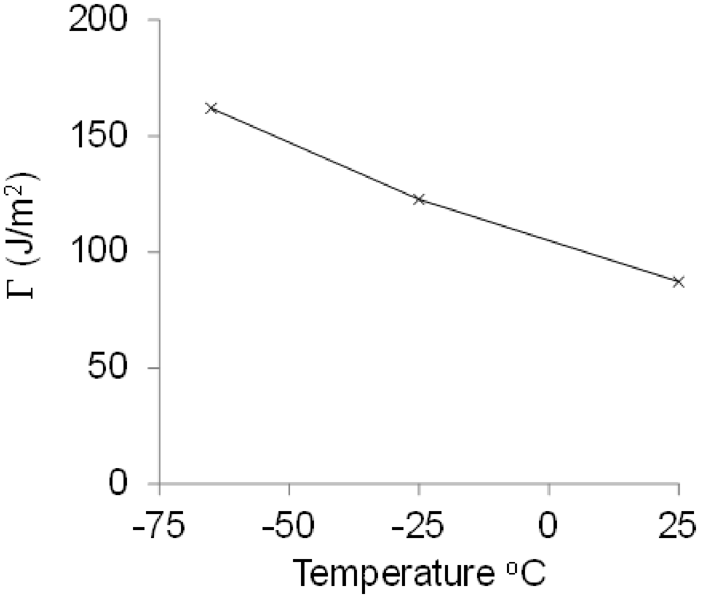

Figure 2-1. Measured temperature-dependent interfacial toughness ($\psi_{r=0.10\ mm}$ = -20^o).

3. NLVE SPEC EPOXY MODEL

3.1 Polymer modeling

Glassy polymers exhibit behavior quite different from metals and ceramics. They undergo nonlinear, time-dependent relaxations in volume and stress that define a glass transition when heating or cooling between the rubbery and glassy state of the material. During that transition, properties can change significantly. It is not uncommon for the effective thermal expansion coefficient to experience a threefold change in magnitude while the shear modulus changes by a couple orders of magnitude. This is particularly important in electronic packaging where polymers often are used to encapsulate or underfill printed wiring board components. There the mismatch in thermal strains and material stiffness across bonded interfaces can generate high stresses leading to cohesive cracking, adhesive debonding or thermal fatigue in critical solder joints. Modeling provides a means to avoid premature component failures through systematic analyses guiding the development of robust designs and manufacturing processes. However, this requires an accurate material model capable of predicting the full range of polymeric behavior under general thermal-mechanical environments.

Potential Energy Clock (PEC) model

A physically based polymer model must meet certain well-defined criteria drawn from experimental observations. The intrinsic time dependence arises from an underlying relaxation mechanism that has been shown to conform to the time-temperature hypothesis of Leaderman (Leaderman 1943). Dissipation, history dependence with fading memory, glass transition, a sensitivity to temperature and a "yield-like" behavior producing highly nonlinear relaxations under relatively high stress or strain all strongly favor a nonlinear viscoelastic modeling approach over elasticity or plasticity. The thermorheologically simple behavior (Schwarzl and Staverman 1952) is captured readily with a material clock described by the WLF equation (Williams, Landel et al. 1955) in the small strain regime for the equilibrated material above glass transition. However, a nonlinear, thermodynamically consistent formalism is needed to predict properly the acceleration in relaxation rates under finite strains.

To meet these requirements, Caruthers et al. (Caruthers, Adolf et al. 2004) developed a nonlinear viscoelastic formalism whereby the Helmholtz free energy was represented by a second order Frechet series expansion in the temperature and strain histories for a material undergoing finite deformations with fading memory employing a material clock. The proposed Helmholtz free energy served as a potential function from which the stress constitutive equation was derived along with other thermodynamic quantities of interest (e.g., entropy, internal energy). The success of the constitutive framework was secured by two important findings. The first was the identification of the Hencky strain as the appropriate strain measure for the second order expansion. This requirement arose from the need for the first invariant of the strain tensor to be a function of volume only to achieve the incompressibility limit as the material transitioned from the glass into the rubber. The second critical aspect of the model was determining the driving force for the material clock. That was found to be the potential part of the internal energy.

The Potential Energy Clock (PEC) model was shown to predict a broad range of relaxation phenomena for both thermosets and thermoplastics including temperature and time dependence of stress-strain through "yield", volume and enthalpy relaxation and stress relaxation during multi-step loading histories (Adolf, Chambers et al. 2004). Moreover, this was accomplished using a single set of PEC material parameters for each material. There are, however, intrinsic difficulties associated with the use of the PEC model. First, being formulated in terms of the Hencky stress-strain relations, the finite element implementation of the model requires a fourth order tensor transformation to map the logarithmic stress-strain equations into the Cauchy space. This is computationally taxing. Second, there are single and double hereditary integrals requiring four independent relaxation functions stemming from the entropy definition and the volume, shear, and temperature terms in the definition of stress. Although the model is populated exclusively from linear viscoelastic properties using no phenomenological tuning parameters, these viscoelastic functions, properties and all the associated temperature/volume dependencies must be measured accurately and consistently. That requires an extensive experimental characterization that is time consuming and prohibitively expensive for most engineering applications.

Simplified Potential Energy Clock (SPEC) model

To ease the experimental and computational burdens imposed by the PEC formalism, a simplified potential energy clock (SPEC) model (Adolf, Chambers et al. 2009) was developed. This was accomplished by a combination of steps intended to reduce the complexity of the numerical computations, avoid some of the higher order temperature and volume dependencies and make the material clock more phenomenological by introducing "fitting" parameters. To bypass the calculations of a logarithmic strain and the fourth order tensor transformation needed to compute the Cauchy stress, the Hencky strain rate was approximated by the unrotated rate of deformation tensor, *d*. Although the integral of the rate of deformation tensor does not yield a true strain measure, it does provide a very close approximation to the Hencky strain for strain levels that would be reasonable for a glassy polymer. The resulting SPEC approximation for the Cauchy stress, σ, is

$$\begin{aligned}
\underline{\underline{\sigma}}(t) = {} & \frac{\rho}{\rho_{ref}}\left[\Delta K(T)\int_0^t ds\, f_v\left(t^* - s^*\right)\frac{dI_1}{ds} - \Delta A(T)\int_0^t ds\, f_v\left(t^* - s^*\right)\frac{dT}{ds}\right]\underline{\underline{I}} \\
& + \frac{2\rho\,\Delta G(T)}{\rho_{ref}}\int_0^t ds\, f_s\left(t^* - s^*\right)\left[\underline{\underline{R}}(t)\cdot\underline{\underline{d}}_{dev}(s)\cdot\underline{\underline{R}}^{-1}(t)\right] \\
& + \frac{\rho}{\rho_{ref}}\left[K_\infty(T)I_1(t) - A_\infty(T)\{T(t) - T(0)\}\right]\underline{\underline{I}} \\
& + \frac{2\rho\, G_\infty(T)}{\rho_{ref}}\left[\underline{\underline{R}}(t)\cdot\underline{\underline{\varepsilon}}_{dev}(t)\cdot\underline{\underline{R}}^{-1}(t)\right]
\end{aligned} \qquad (3\text{-}1)$$

In this equation, ρ and ρ_{ref} are the densities at the current state and reference state, f_v and f_s are normalized volumetric and shear relaxation spectra which decay from 1 to 0, *R* is the rotation tensor, $\underline{\underline{I}}$ is the identity tensor, ε is the strain computed from the integral of the rate of deformation tensor, I_1 is the trace of the strain tensor, *T* is temperature, and the “dev” subscript denotes the deviatoric part of the designated tensor. The prefactors in the above equations are parameters that must be determined for each specific material. In general, they are related but not identically equal to the more commonly recognized bulk and shear moduli, *K* and *G,* and volumetric thermal expansion coefficient, α, as follows. A temperature dependence in these prefactors, denoted by (*T*) in the equations below, is allowed.

$$\Delta K(T) = K_g(T) - K_\infty(T) \tag{3-2}$$

$$\Delta G(T) = G_g(T) - G_\infty(T) \tag{3-3}$$

$$\Delta A(T) = \left[K_g \alpha_g - K_\infty \alpha_\infty\right](T) \tag{3-4}$$

The subscripts "∞" and "*g*" are applied to designate the "equilibrium" and "glassy" values of a designated parameter. The material clock is defined by a shift factor, "*a*", based on a re-definition of the potential energy found in the PEC model.

$$t^* = \int_0^t \frac{dw}{a(w)} \tag{3-5}$$

$$\log\left[a(t)\right] = -\frac{C_1 N(t)}{C_2 + N(t)} \tag{3-6}$$

$$\begin{aligned} N(t) = &\left\{\left[T(t) - T_{ref}\right] - \int_0^t ds\, f_v\left(t^* - s^*\right) \frac{dT}{ds}(s)\right\} \\ &+ C_3 \left\{I_1(t) - \int_0^t ds\, f_v\left(t^* - s^*\right) \frac{dI_1}{ds}(s)\right\} \\ &+ C_4 \left\{\int_0^t ds\, f_s\left(t^* - s^*\right) \underline{\underline{d}}_{dev}(s)\right\} : \left\{\int_0^t ds\, f_s\left(t^* - s^*\right) \underline{\underline{d}}_{dev}(s)\right\} \end{aligned} \tag{3-7}$$

The coefficients C_1 through C_4 are phenomenological and must be fit to data. For an equilibrated material undergoing free thermal expansion/contraction above the glass transition temperature, the integrals are identically zero and the material clock depends on temperature and volume only.

Although the experimental characterization and model calibration process is easier for the SPEC model than the PEC model, the performance predictions are quite comparable. The SPEC approximations have been shown to be entirely suitable for engineering applications (Adolf, Chambers et al. 2009) having been applied to unfilled thermosets and thermoplastics as well as epoxies with particulate fillers that were characterized as an isotropic homogeneous continuum. Note that the PEC and SPEC models both assume a fully cured, stress-free material at the end of cure.

Material characterization and SPEC model calibration procedures

Perhaps the most formidable challenge of viscoelastic modeling arises from the time, expense and difficulty in performing the requisite material characterization and model calibration. In general, the SPEC model requires data to define the two relaxation spectra, the decaying prefactors for the hereditary integrals and the corresponding equilibrium parameters. This leads naturally to three classes of experiments involving shear, temperature and volume.

The shear tests are relatively straightforward. The glass transition temperature (T_g) and modulus temperature dependence can be obtained with a Dynamic Mechanical Analyzer (DMA) measuring the storage and loss moduli during torsion at fixed frequency while sweeping the temperature at a constant rate from the glassy to the rubbery states. The shear master curve is built following the conventional approach for thermorheologically simple materials. Here, the DMA test protocol is changed to measure dynamic properties across a range of frequencies during isothermal tests conducted at different temperatures taken around glass transition. At each temperature, the shear storage and loss moduli, G' and G'' respectively, are measured and tan δ is computed as the ratio of the two values (tan $\delta = G''/G'$). These data then are plotted versus the logarithm of frequency producing a family of curves, one for each test temperature. The master curve is generated from the tan δ plots by first choosing a reference temperature (T_{ref}) curve and horizontally shifting all remaining curves on the log frequency axis to obtain a smooth, continuous, composite representation of the function. By performing the horizontal shifts with the tan δ curves, the modulus temperature dependence cancels out and the need for vertical shifts is removed. Once the horizontal shift factors have been defined from the tan δ curves, the master curves for storage and loss moduli are constructed by applying the same horizontal shifts. In this case, some vertical shifts may be necessary to accommodate small changes in moduli with temperature. Although this produces master curves in the frequency domain, viscoelastic analyses utilize relaxation functions in the time domain. That requires an additional mapping facilitated by an exponential series expansion (Prony series) providing a convenient representation for the shear relaxation spectrum as follows:

$$G(t) = G_\infty + \Delta G \sum_{i=1}^{N} f_i \exp\left(-t/\tau_i\right) = G_\infty + \Delta G f_s(t) \qquad (3\text{-}8)$$

The values f_i and τ_i are fitting constants. When the exponential series is substituted into the linear viscoelastic shear hereditary integral and the stress is computed for a sinusoidal, constant amplitude shear strain history, $\gamma_o \sin(\omega t)$, expressions are obtained for the storage and loss moduli in terms of the exponential series parameters and the frequency, ω:

$$G'(\omega) - G_\infty = \Delta G \sum_{i=1}^{N} f_i \left(\omega\tau_i\right)^2 / \left[1 + \left(\omega\tau_i\right)^2\right] \qquad (3\text{-}9)$$

$$G''(\omega) = \Delta G \sum_{i=1}^{N} f_i \left(\omega\tau_i\right) / \left[1 + \left(\omega\tau_i\right)^2\right] \qquad (3\text{-}10)$$

The latter two equations are suitable for fitting the shear storage and loss master curves in the frequency domain. When the fitting constants are defined, the relaxation spectrum in the time domain is computed directly from Equation 3-8.

The bulk modulus and its temperature dependence can be measured with a pressure-dilatometer. This often is achieved by applying strain gauges to a protected sample pressurized in a fluid bath. Mapping the bulk relaxation spectrum, f_v, directly by measuring the time dependence of the decaying pressure following step changes in volume at different temperatures is much more cumbersome. Fortunately, there is an alternative resulting from the fact that the SPEC model uses a single relaxation function for both the bulk and temperature hereditary integrals. Thermal strain data collected with a Thermal Mechanical Analyzer (TMA) provide another means of calibrating the model. Since the location and shape of the glass transition are determined by the prescribed temperature history, a properly calibrated constitutive equation must be able to predict the heating and cooling strains from an analysis of the actual test conditions. That suggests the possibility of using an iterative modeling approach to deduce the prefactors and relaxation function required to minimize the error between predictions and data. Starting from an assumed property set, the SPEC model is used to predict the thermal strain response during a temperature history cycling through glass transition at prescribed rates. The resulting strain-temperature curves are compared to the measured data, and model parameters are adjusted to minimize the error. The slopes of the glassy and rubbery response contribute to the definition of the prefactors in Equations 3-2 and 3-4. The parameterization of the relaxation function is facilitated by simplifying the functional form to a stretched exponential. This allows the minimization of error from the relaxation function to be controlled through the specification of only two parameters, λ and β:

$$f_v(t) = \exp\left(-(t/\lambda)^{\beta}\right) \tag{3-11}$$

In general, the stretched exponential still must be converted to a Prony series for ease of constitutive computations. However, by specifying a fixed distribution of relaxation times, the Prony prefactors are solved readily from a linear set of equations. Surprisingly, the iterative process of parameterization works very well and is easily executed with a finite element analysis in a one-element problem.

Through a judicious choice of C_1 and C_2, the material clock equation for the logarithm of the shift factor can be reduced to the familiar WLF form for an equilibrated material. The C_3 parameter defines the pressure dependence of the glass transition temperature while C_4 governs the nonlinear relaxations producing “yield-like” behavior under loading. The C_4 parameter is chosen to reproduce stress-strain data conducted at several different temperatures.

Epoxy data and SPEC model parameters

The primary epoxy chosen for this study was 100 pbw digylcidyl ether of bisphenol A (Epon 828) with 43 pbw polyether amine Jeffamine T403 cured 24 hours at 80°C. To provide data on the temperature dependence of the glassy shear modulus, beams with a rectangular cross-section were subjected to oscillatory torsion under small strains at 1 Hz as the sample was heated from -60°C to 100°C at 2°C/min. The shear storage modulus, *G’* was measured at Sandia for samples that had been quenched and slow cooled to ascertain the role of conditioning. Additional data was available from a contracted source. These data are plotted in Fig. 3.1. Although the SPEC model assumes a linear change in modulus with temperature, the data show nonlinearities at the lower temperatures. The contracted data cover a much more limited temperature range and differ quantitatively in magnitude. The range in d*G'*/d*T* above 0°C seems to vary from about -2 to -5 MPa/°C. For comparison, Epon 828/DEA epoxy has a value of about -4 MPa/°C. Since there are other experiments and predictions affected by d*G'*/d*T*, the calibrated magnitude was refined further by blending the errors between all model predictions and data.

Following the procedure described in the previous section, the shear storage, *G'*, and loss, *G''*, moduli were measured as a function of frequency at constant temperatures across a range of temperatures varying from 30°C to 120°C in increments of 5°C. The ratio of *G''* to *G'* (tan δ) was constructed for use in shifting tan δ curves relative to a reference temperature of 90°C to obtain the WLF shift factors. These shift factors were then applied to the storage and loss data. It is these master curves that are fit by Equations 3-9 and 3-10 to obtain the Prony series coefficients for the SPEC shear stress relaxation modulus. The resulting master curves and Prony series fits in frequency space are plotted in Fig. 3-2 and Fig. 3-3. The corresponding shear relaxation modulus obtained from Equation 8 is plotted in Fig. 3-4.

Thermal strain data were collected from Thermal Mechanical Analysis (TMA) measured on samples heated and cooled at 3°C/min. A set of parameters were assumed for Eq. 3-11 and the experiment was analyzed using the SPEC model to predict the thermal strains. Through an iterative procedure comparing model results to data, the values of β and τ were chosen to minimize the strain errors. A plot of the thermal strain data and calibrated SPEC model is provided in Fig. 3-5.

The final set of data used in the SPEC model calibration comes from compression stress-strain curves conducted at various temperatures. All samples were annealed at 110°C for 15 minutes and cooled to room temperature at 2°C/min. Samples then were placed in an oven at the test temperature for 15 minutes before applying the deformation at about 5% strain/min. The tests were analyzed using the SPEC model calibration determined from the master curve construction along with the data collected on the volume relaxation response captured from the thermal strain versus temperature data. The magnitude of the yield stress was used to calibrate the final value of dG_g/dT and the clock parameter C_4. The pressure dependence of the glass transition temperature was approximated by defining C_3 to create a shift in T_g of about 20°C per 100 MPa of pressure.

Plots of the comparisons between the calibrated SPEC model and test data are provided in Figures 3-6 to 3-9 for temperatures -25, 0, 25 and 45°C. The SPEC model parameters for this epoxy, which is referred to as EPON 828/T403 are defined in Table 3-1.

Note that analysis described in section 4 were performed using the SPEC fit for another epoxy referred to as Epon828/DEA: 100 pbw digylcidyl ether of bisphenol A (Epon 828) with 12 pbw diethanolamine. These calculations were performed early in the program prior to the availability of the EPON828/T403 SPEC fit. The SPEC properties for Epon828/DEA are documented in Table 3-2.

3.2 Illustrative Epon 828/T403 NLVE results as predicted by the SPEC model

The Epon 828/T403 NLVE SPEC model can be used to estimate the epoxy's temperature-dependent elastic and yield properties. Note that in a NLVE material model, elastic properties such as E, ν, and apparent yield strength σ_y do not have a fixed value, but should be thought of as calculated, history dependent, derived quantities. The apparent elastic properties and yield strength of a NLVE material can be estimated by performing one-element, finite element analysis (FEA) calculations where the material is first cooled to a prescribed temperature that is well below the material's glass transition temperature T_g (i.e., deep into the glassy regime) and is then uniformly stressed by applying a mechanical load (e.g., in tension). These calculated values depend on the cooling rate, the temperature at which the mechanical loads are applied, and the applied strain rate. Such calculations were performed using the SPEC NLVE constitutive model for Epon 828/T403 to estimate its elastic properties and yield strength at 25^{o}C, 0^{o}C, -25^{o}C and -50^{o}C for a prescribed cooling rate of 2^{o}C/min and an applied strain rate of 0.01/s (see Table 3-3). The predicted Young's modulus and the apparent yield strength (i.e. peak stress in calculated stress-strain curve) increases linearly with decreasing temperature (Figs. 3-10 and 3-11). Modulus increases by ~ 20% while the yield strength increase by ~ 80% as temperature is decreased from 25^{o}C to -50^{o}C. Tensile/compression/shear results also show that a von Mises yield criterion appears to be an acceptable choice. Note that experimentally measured RT compression properties (as reported in section 2.1) are E=3.15 GPa, ν=0.39 and σ_y=80 Mpa. The measured yield strength is close to that calculated, while the measured E is ~ 20% higher than calculated value.

Finally note that the NLVE SPEC model can generate material softening that can lead to strain localization. Figure 3-12 plots the nominal engineering stress-strain response of a cylindrical plug subjected to a compressive load. Two cases were considered: 1) a straight-sided cylinder with fully bonded boundary condition applied to the ends of the cylinder and 2) a tapered cylinder with an initial 1% diameter reduction at its center and with frictionless boundary conditions applied on its ends. As shown in Fig. 3-12, both cases predict bulging associated with strain localization. This localization is initiated by a stress perturbation (either by perturbing the geometry or perturbing the uniformity of the loading). The portion of the computed stress-strain curve that occurs after peak load is therefore specimen dependent; one-element calculations can only generate useful results prior to localization.

Table 3-1. SPEC Model Parameters for Epon 828/T403

K_g (GPa)	4.9
dK_g/dT (MPa/°C)	-12
K_{eq} (GPa)	3.5
dK_{eq}/dT (MPa/°C)	-12
β_g (ppm/°C)	265
$d\beta_g / dT$ (ppm/°C/°C)	0.6
β_{eq} (ppm/°C)	500
$d\beta_\infty / dT$ (ppm/°C/°C)	0.9
G_g (GPa)	0.75
dGg/dT (MPa/°C)	-2.7
T_{ref} (°C)	90
C_1	16.5
C_2	79.025
C_3	900
C_4	30000
$f_1(t)$	$\exp\left(-\left(t/0.001\right)^{0.20}\right)$
$f_2(t)$	$\exp\left(-\left(t/0.1\right)^{0.25}\right)$

Table 3-2. SPEC Model Parameters for Epon 828/DEA

K_g (GPa)	4.9
dK_g/dT (MPa/°C)	-12
K_{eq} (GPa)	3.2
dK_{eq}/dT (MPa/°C)	-12
β_g (ppm/°C)	170
$d\beta_g / dT$ (ppm/°C/°C)	0.2
β_{eq} (ppm/°C)	600
$d\beta_\infty / dT$ (ppm/°C/°C)	0.4
G_g (GPa)	0.90
dGg/dT (MPa/°C)	-4.2
G_{eq} (MPa)	4.5
T_{ref} (°C)	75
C_1	16.5
C_2	87.2
C_3	1000
C_4	11800
$f_1(t)$	$\exp\left(-\left(t/6\right)^{0.14}\right)$
$f_2(t)$	$\exp\left(-\left(t/0.12\right)^{0.22}\right)$

Table 3-3. NLVE Epon 828/T403 SPEC model estimates for temperature-dependent elastic and yield properties.

°C	loading	E (MPa)	ν	G (MPa)	σ_y (MPa)
25	tension	2620	0.42	920 [b]	83
	compression	2620	0.42	920 [b]	89
	shear			920	85 [a]
0	tension	2810	0.42	990 [b]	106
	compression	2820	0.42	990 [b]	113
	shear			990	108 [a]
-25	tension	3000	0.42	1060 [b]	129
	compression	3010	0.42	1060 [b]	136
	shear			1060	130 [a]
-50	tension	3200	0.42	1130 [b]	152
	compression	3200	0.42	1130 [b]	159
	shear			1130	152 [a]

[a] Converted calculated τ_y to σ_y using $\tau_y=\sigma_y/3^{1/2}$.

[b] Calculated shear modulus G using $G=0.5E/(1+\nu)$

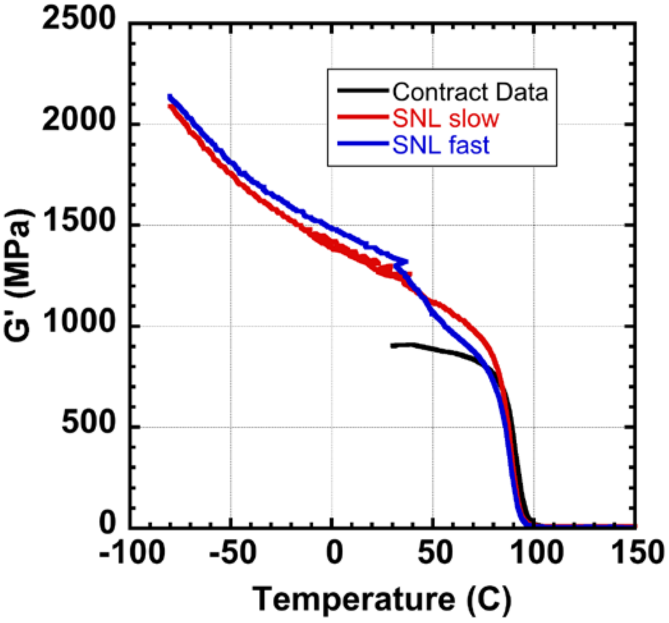

Figure 3-1. 828T403 shear storage modulus measured at 1 Hz while heating at 2°C/min.

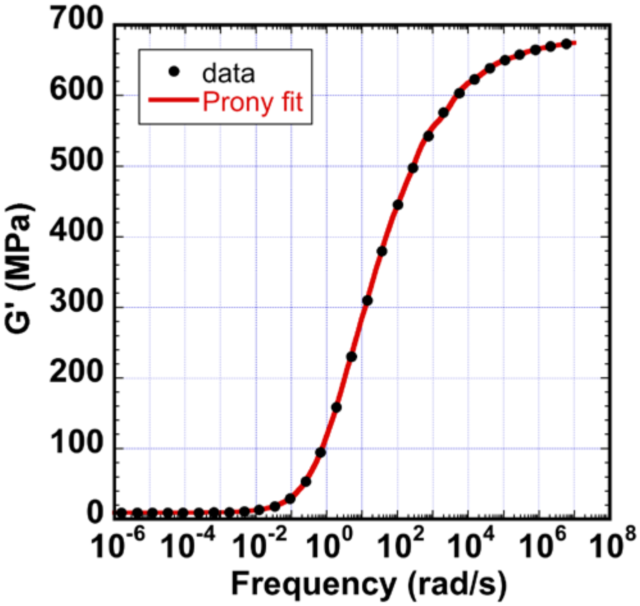

Figure 3-2. 828T403 shear storage modulus master curve data and corresponding Prony series fit for reference temperature equal to 90°C.

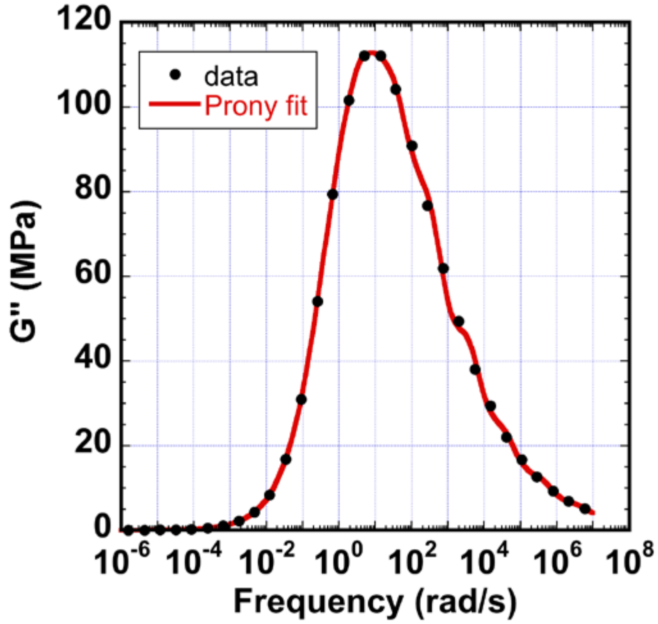

Figure 3-3. 828T403 shear loss modulus master curve data and corresponding Prony series fit for reference temperature equal to 90°C.

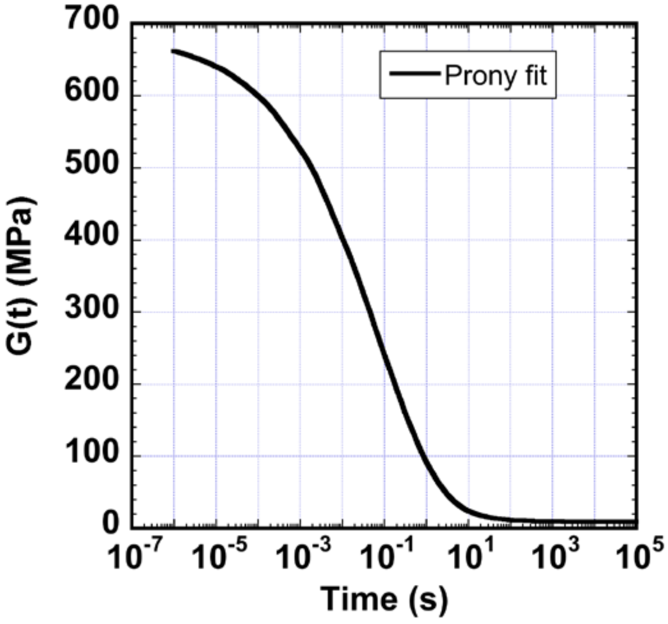

Figure 3-4. 828T403 shear stress relaxation function at reference temperature equal to 90°C.

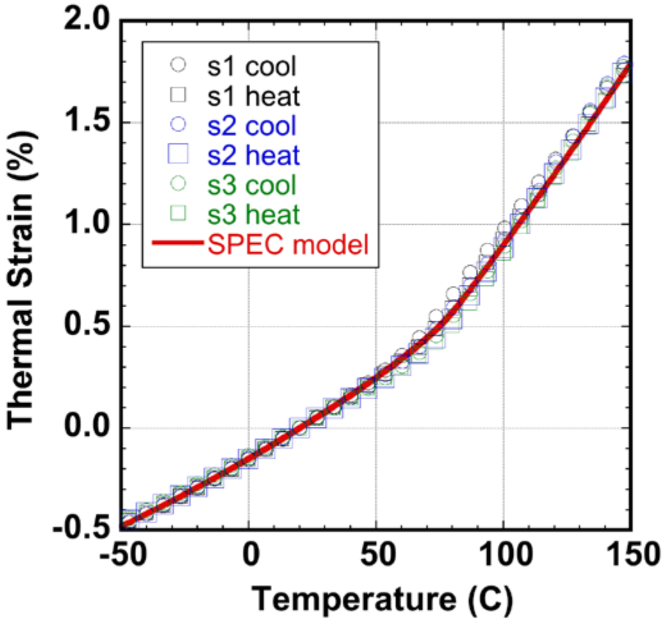

Figure 3-5. Comparison of calibrated SPEC model and thermal strain data for 828T403 epoxy heated and cooled at 3 C/min.

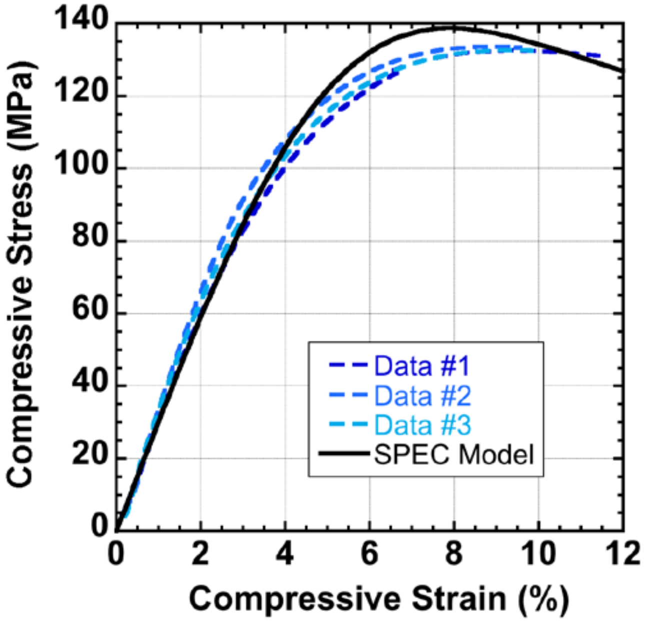

Figure 3-6. Comparison of calibrated SPEC model and data for 828T403 at T=-25°C.

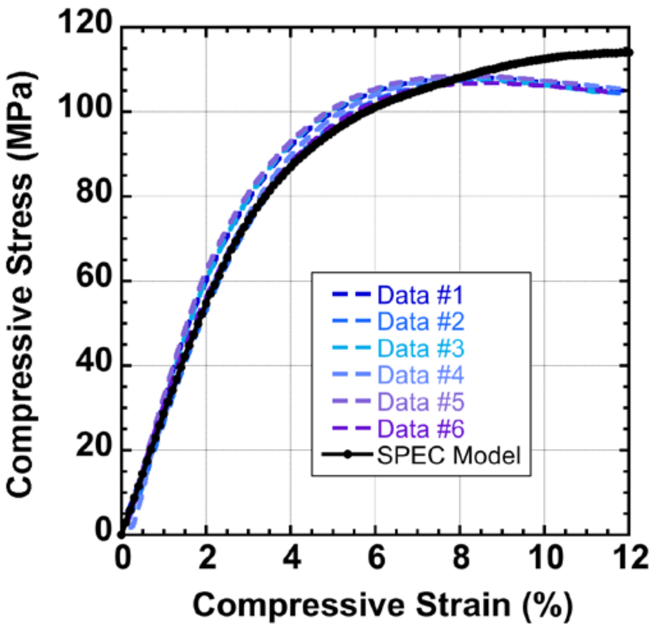

Figure 3-7. Comparison of calibrated SPEC model and data for 828T403 at T=0°C.

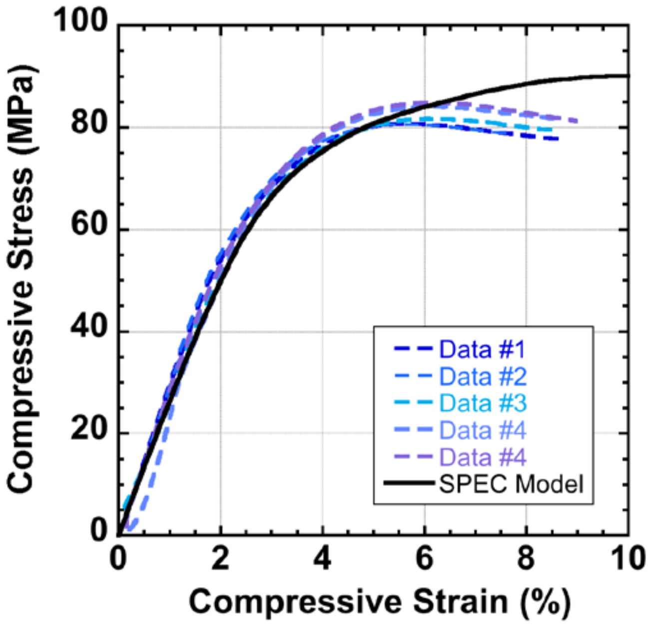

Figure 3-8. Comparison of calibrated SPEC model and data for 828T403 at T=25°C.

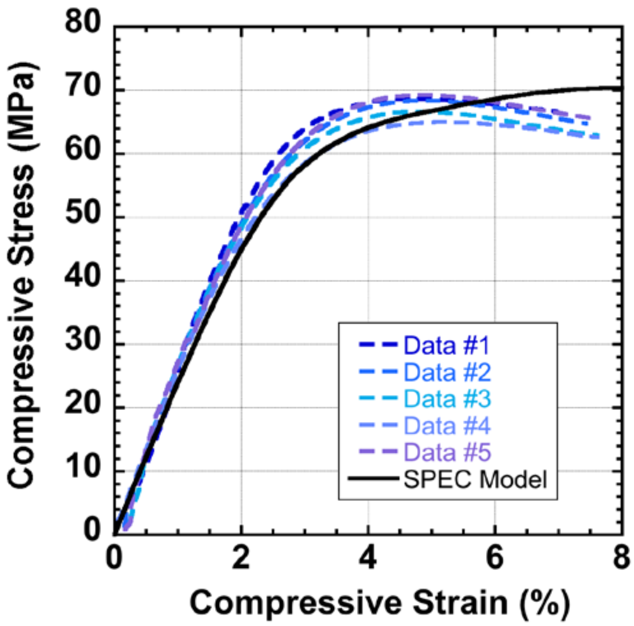

Figure 3-9. Comparison of calibrated SPEC model and data for 828T403 at T=45°C.

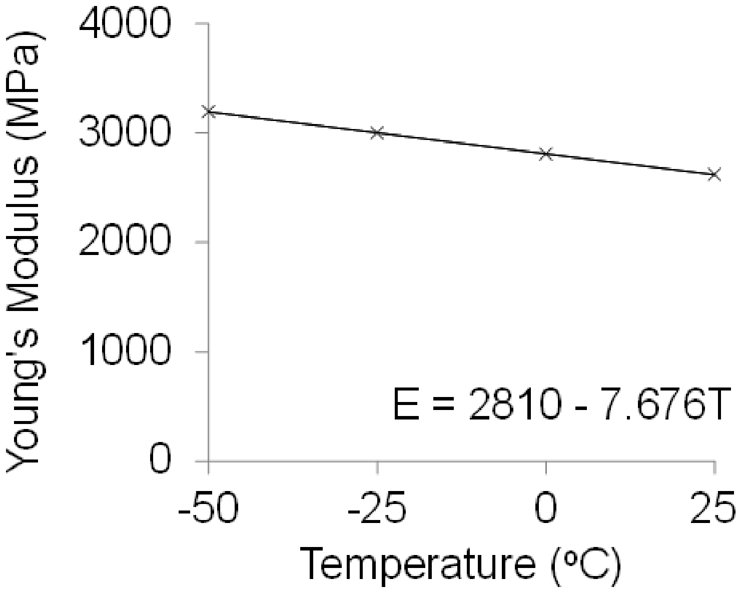

Figure 3-10. Predicted temperature-dependent *E* for a prescribed cooling rate of 2^{o}C/min and an applied strain rate of 0.01/s.

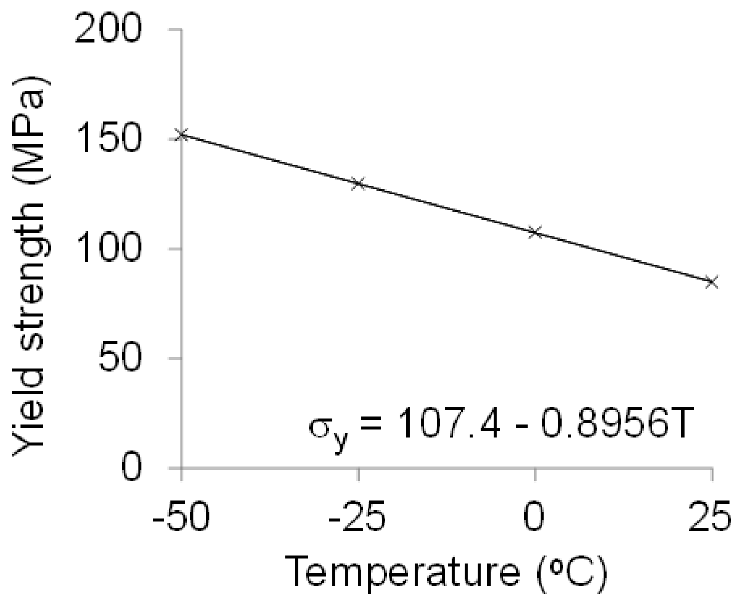

Figure 3-11. Predicted temperature-dependent σ_y for a prescribed cooling rate of 2°C/min and an applied strain rate of 0.01/s.

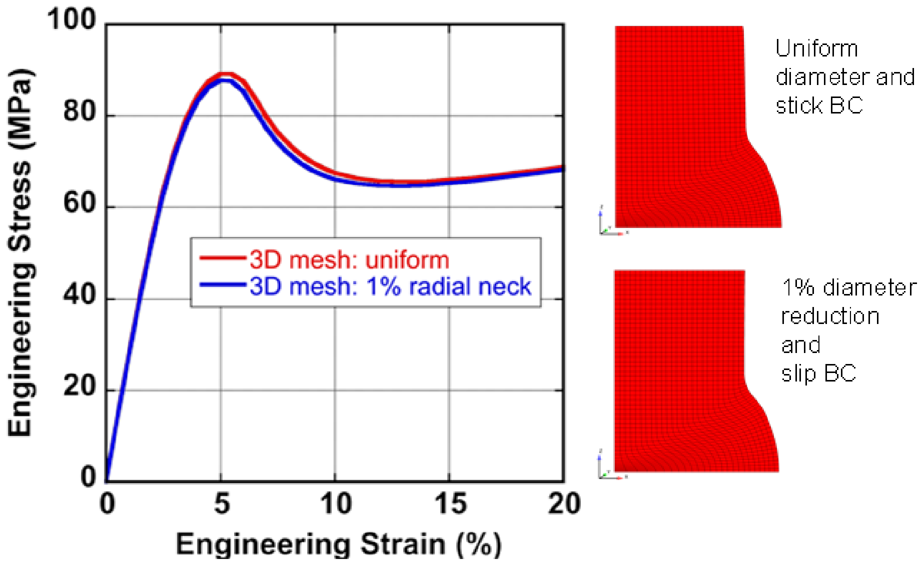

Figure 3-12. Predicted compressive stress-strain curves for straight-sided cylinder with stick boundary condition and also for a cylinder with an initial 1% diameter reduction and a frictionless boundary condition.

4. NLVE ANALYSIS OF AN ADHESIVELY BONDED BUTT JOINT

A simple, prototypical crack initiation problem will be considered in this section: the rigid adherend, adhesively bonded butt joint subjected to a tensile load (Fig. 4-1). There is no pre-existing crack in this plane strain analysis. Nonetheless, interfacial normal and shear stress exhibit a steep stress gradient as the stress-free edge is approached. Indeed, within the context of elasticity theory the stress is singular at the interface corner (where the interface meets the stress-free edge). The elasticity solution will be presented first, followed by finite element results from analyses that use the NLVE SPEC model for the adhesive.

4.1 Background: Linear elastic analysis of an adhesively bonded butt joint with rigid adherends

The asymptotic, plane strain elasticity solution for a rigid adherend butt joint with a thin elastic bond has been derived during previous work (Reedy 1990; Reedy 1993). Results are available for both a tensile loading and also for a uniform layer shrinkage (e.g., as a result of a uniform temperature change). The solution for the interfacial normal stress σ_n and interfacial shear σ_t is

$$\begin{aligned} \sigma_n &= K_a r^{-\delta} + \sigma_{\mathrm{n}}^{\mathrm{o}} \\ \sigma_t &= cK_a r^{-\delta} \\ \\ K_a &= \hat{\sigma} h^{\delta} A_p \\ \hat{\sigma} &= \frac{\nu}{1-\nu}\sigma_n^{*} - \frac{E\varepsilon_o^{*}}{1-\nu} \\ \sigma_{\mathrm{n}}^{\mathrm{o}} &= \frac{E\varepsilon_o^{*}}{\nu} \end{aligned} \tag{4-1}$$

where σ_n^{*}= applied tensile stress, ε_o^{*}= shrinkage strain (e.g., introduced by a uniform temperature change), $2h$ = bond thickness, E = Young's modulus, r = distance from interface corner, and A_p,c, and δ depend on Poisson's ratio ν. When ν= 0.35, A_p=0.958, c=-0.35, and δ= 0.32.

4.2 Baseline butt joint problem

Figure 4-2 shows the finite element mesh used in the calculations. The adherends are 14.3 mm high x 28.6 mm wide in this plane strain analysis, and the adhesive bond is one mm-thick (analyzed a one-quarter model of the butt joint with symmetry conditions applied). A highly refined, focused mesh is used at the interface corner where the minimum element size Δ was chosen so that Δ/h~ 0.0003. The adherend stiffness was chosen so that it was essentially rigid in comparison to the epoxy layer (E~3000 times that of the epoxy) and the adherend's coefficient of thermal expansion is zero. The bond is modeled using the NLVE SPEC model for an Epon 828/DEA epoxy (Table 3-2). In this baseline calculation, the epoxy is cooled from 75°C to 25°C in 600 sec. The adherend is free to move in the axial direction during cooling (no net bond normal interfacial load generated during cooling). After cooling, a bond normal tensile load is applied until the nominal bond-normal strain is 0.003 (uniformly displacement U^* applied to upper adherend at a strain rate of 0.0005/s for 6 seconds). The elastic properties used in the comparative linear elastic asymptotic interface corner predictions (using Eq. 4-1) were determined by matching the bond stress that the NLVE analysis predicts to occur in the joint's uniformly stressed interior as calculated at the end of the cooling step as well as at a subsequent tensile increment (i.e., at 25^{o}C and strain rate of 0.0005/s, E=2.86 GPa, ν=0.41, and α = 55e-5/^{o}C). A linear elastic uniaxial strain analysis that uses these values of E, ν, and α will generate the same transverse stress at the end of the cooling step as is determined by a NLVE uniaxial strain calculation when a reference temperature 75^{o}C is used.

Calculated results for the baseline problem suggest "small-scale yielding-like" behavior (Fig. 4-3). The asymptotic interface corner solution (Eq. 4-1) dictates that a ln-ln plot of σ_n-σ_n^o vs. distance from the interface corner r plots as a straight line with a slope equal to the strength of the interface corner singularity (when ν=0.41, δ=0.36) when the material response is linear elastic. The plotted NLVE results suggest that there is a "yield zone" embedded within the singular stress field predicted by a linear elastic analysis. The size of the region of dominated by highly nonlinear material response is a few μms long (i.e., length of the yield zone). For comparison, a typical grit-blasted aluminum surface has an RMS surface roughness of ~ 5 μm. This suggests that linear elastic fracture mechanics concepts such as small-scale yielding might be applicable (see replot, Figure 4-4).

4.3 Variations from baseline calculation

Additional calculations were performed to examine the effect of varying cooling history when cooling from 75^{o}C to 25^{o}C (i.e., prior to application of tensile load). In the baseline calculation, cooling occurs over a period of 600 seconds. Two alternate cooling histories were considered: 1) cooling in 6000 seconds, and 2) cooling in 600 seconds, but cooling is followed by a 10e5 second hold prior to applying the tensile load. Figure 4-5 shows that the interfacial normal stress is essentially identical for all three cooling histories. Other calculations examined the effect of varying the tensile loading rate after cooling from 75^{o}C to 25^{o}C in 600 seconds. In the baseline calculation, the load was applied in 6 seconds. In alternate calculations the load was applied either 10 times faster or 10 times slower. The calculated interfacial normal stress distribution show little change with loading rate (Fig. 4-6).

In a final set of results, the effect of decreasing the temperature prior to application of tensile load was examined (i.e., increasing residual stress). In the baseline calculation, the epoxy is cooled from 75^{o}C to 25^{o}C at a rate of 2^{o}C/min. prior to application of the tensile load (U^*=0.003). In an alternate calculation, the epoxy is cooled from 75^{o}C to -25^{o}C at a rate of 2^{o}C/min. prior to application of the tensile load (U^*=0.003). Figure 4-7 plots the normalized interfacial shear stress (normalized by the characteristic stress σ^*, see Eq. 4-1) vs. the normalized distance from the interface corner. Note that the asymptotic linear elastic interface corner solution indicates that when the bond material is linear elastic, the interfacial shear stress distribution should scale with the characteristic applied stress $\hat{\sigma}$, and the slope of a ln-ln plot of σ_t vs.r should equal the strength of the interface corner singularity (when ν=0.41, -δ=-0.36). The plotted NLVE results suggest "small-scale yielding-like" behavior for both levels of cooling (as shown on the figure, curve fits generate slopes of -0.34 and -0.35). Also note that $\hat{\sigma}$ is the sum of terms associated with uniform shrinkage and mechanical load. When cooled to 25C, ~50% of the value of $\hat{\sigma}$ is associated with cooling, while when cooled to -25C, ~70% of the value of $\hat{\sigma}$ is associated with cooling.

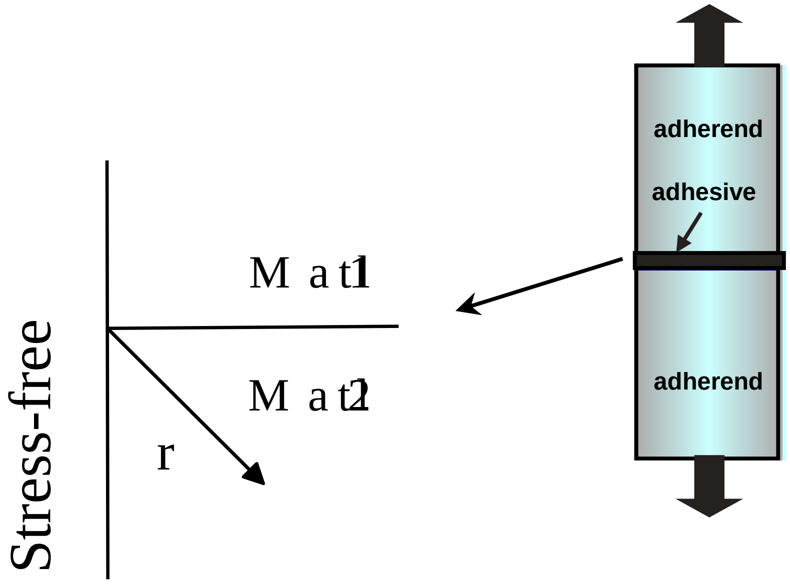

Figure 4-1. Adhesively bonded butt joint and the associated asymptotic interface corner problem.

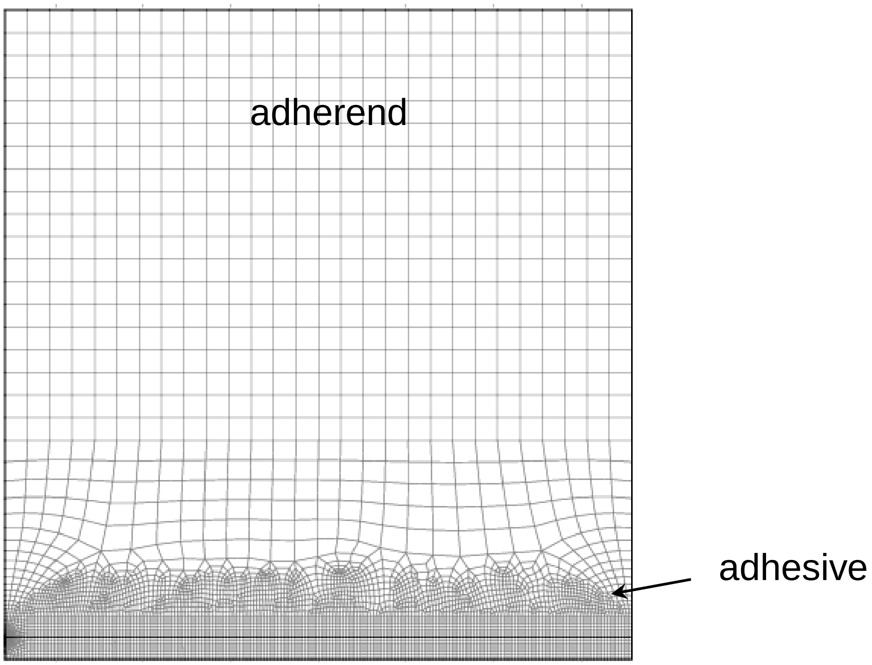

Figure 4-2. Plane strain finite element model of an adhesively bonded butt joint with a 1-mm thick bond and a focused mesh at the interface corner (1/4 model with symmetry conditions).

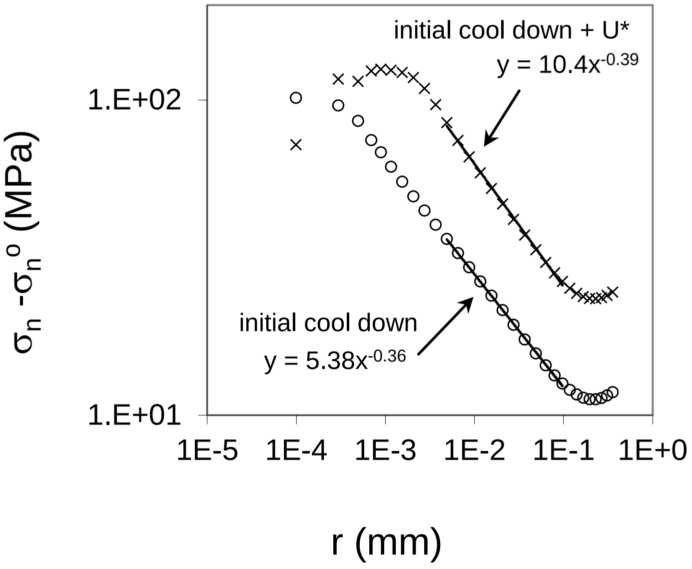

Figure 4-3. Interfacial normal stress prediction for the baseline problem: cool from 75°C to 25°C in 600 seconds followed by a uniform edge displacement that generates a nominal bond-normal strain rate of 0.0005/s for 6 seconds.

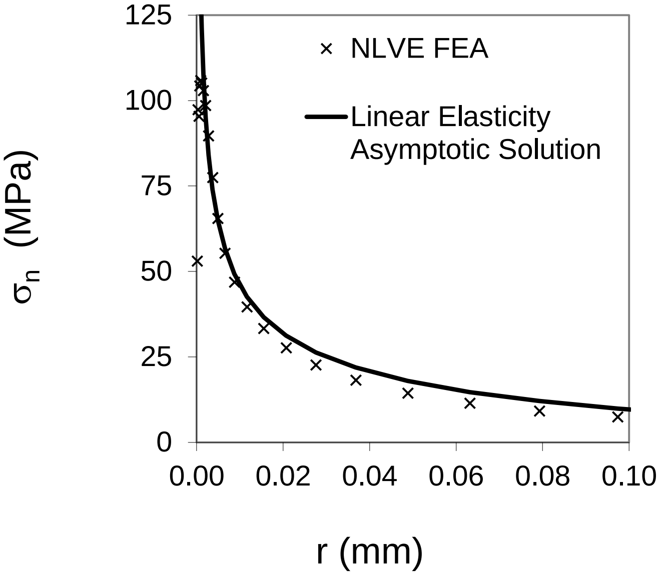

Figure 4-4. Replot of Figure 4-3 results at the end of applied edge loading step along with a comparison to the linear elastic butt joint prediction for interfacial normal stress.

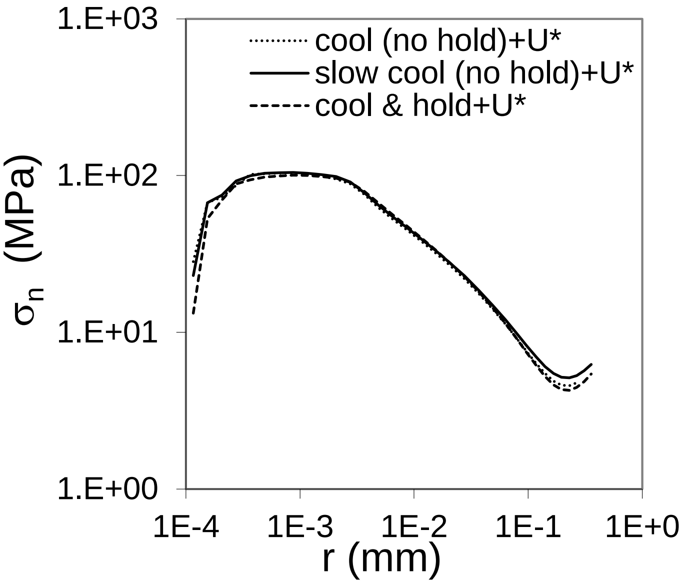

Figure 4-5. Compare baseline interfacial normal predictions with those for a slower cooling rate and also when a 10^5 sec hold is added after cooling and prior to edge loading.

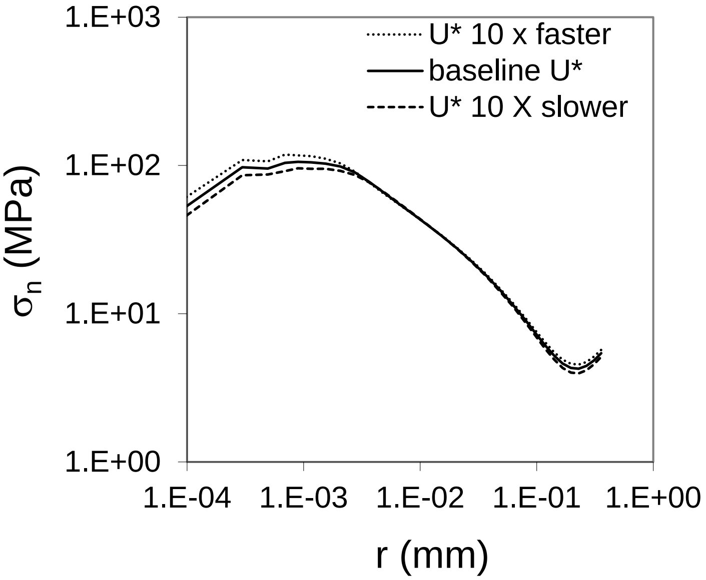

Figure 4-6. Compare baseline interfacial normal stress predictions with those where the edge loading rate is either a 10 times faster or slower.

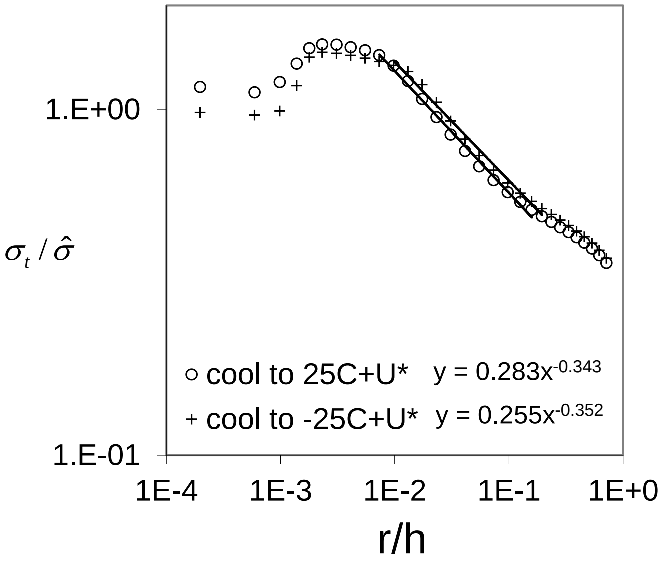

Figure 4-7. Compare baseline interfacial shear predictions where joint is cooled to 25°C with those where the joint is cooled to -25°C prior to edge loading.

5. MODE-MIXITY DEPENDENT COHESIVE ZONE MODEL

5.1 Cohesive zone models for interfacial fracture

A fracture analysis that uses a cohesive zone model (CZM) is computationally attractive for simulating interfacial failure since crack growth is a natural outcome of the solution and the crack path is predefined when fracture is constrained to interfacial separation (i.e., the crack does not kink out of the interface). Moreover, a CZM-based analysis leads to mesh-independent results because a length scale (i.e., separation) is embedded within the model (provided that the mesh is fine enough to resolve the cohesive zone—the region of interfacial softening behind the crack tip, see Fig. 5-1). In a cohesive zone model, interfacial separation occurs in a controlled manner with interfacial tractions resisting interfacial opening. If one considers the idealized case of Mode I-only separation (i.e., adjoining materials are identical and the applied loading is symmetric), interfacial separation can be directly defined by a traction-separation relationship such as shown in Fig. 5-1. The key parameters that define this relationship are the interfacial strength σ^* and the intrinsic work of separation/unit area Γ. In a more general setting, the CZM will couple interfacial normal and shear response since, even under a symmetric loading, the bulk materials adjacent to the interface will typically have different elastic properties and this asymmetry in material properties will induce interfacial shear (Hutchinson and Suo 1992). The relative level of crack-tip shear is typically quantified in terms of the crack-tip mode-mixity $\psi_{r=lo}$. Crack-tip mode mixity is defined by the ratio of interfacial shear σ_{xy} and normal stress σ_{yy} found at a prescribed distance l_o in front of the crack tip, where

$$\psi_{r=l_o} \equiv \tan^{-1}(\sigma_{xy} / \sigma_{yy}) \qquad (5\text{-}1)$$

when the choice of l_o is within the zone of dominance of the K-field (Rice 1988; Cao and Evans 1989; Wang and Suo 1990; Liechti and Chai 1992; Swadener and Liechti 1998; Mello and Liechti 2006).

The measured apparent interfacial toughness of many polymer solid interfaces increases with increasing crack-tip mode-mixity . Furthermore this dependence on mode-mixity can have large impact on observed behavior (Hutchinson and Suo 1992). A mode-mixity dependent toughness can be realized in an analysis that uses a mode-mixity independent CZM if the analysis includes plastic dissipation within the bulk materials that are adjacent to the interface (Tvergaard and Hutchinson 1993). However, this requires a detailed analysis that models nonlinear material behavior at a very fine scale. An alternate approach is to include mode-mixity effects directly in the CZM. In this case the bulk materials could be modeled as linear elastic. Unfortunately, attempts to directly include a mode-mixity dependent toughness in the CZM have proved difficult. For example, in recent work a polynomial-based potential formulation that is defined in terms of four fracture parameters in each fracture mode does replicate a mode-dependent toughness; however, determining all eight fracture parameters is a challenging task (Park and Paulino 2011). In an alternate approach, a nonpotential-based method that defines Mode I and Mode II response independently has been used to model the mode-mixity dependent failure of adhesive joints (Yang and Thouless 2001). This approach uses a mixed-mode failure criterion to link the two independently defined traction-separation relationships.

5.2 A simple mode-mixity dependent cohesive zone model

A simple cohesive zone model that generates a mode-mixity dependent interfacial toughness is described next (Reedy and Emery 2014). This model will be referred to as the mode-mixity dependent toughness cohesive zone model (MDG$_c$ CZM). Roughly speaking, the MDG$_c$ CZM incorporates all sources of crack-tip dissipation where: 1) mode I dissipation is defined by a traction-separation relationship that depends only on normal separation, and 2) mode II (III) dissipation is generated by interfacial shear yielding and slip in the cohesive surface elements that lie in front of the region where mode I softening occurs. The amount of shear dissipation is not defined by a traction-separation relationship; the length of the slip zone is determined by the level of interfacial shear in front of the mode I cohesive zone. This idealized shear response was motivated by the fact that epoxy can exhibit ductile-like response in compression (shear). For example, Figure 5-2 plots engineering stress-strain curves as measured in compression tests of an Epon 828/T403 epoxy (100:43 pbw, cured 24 hr. at 50^{o}C followed by 24 hr. at 40^{o}C). Testing procedures followed the guidelines in ASTM D-695, the Standard Method of Test for Compressive Properties of Rigid Plastics, using 13.1m diameter by 29.2 mm long samples that were loaded at a nominal strain rate of 0.00027/s. The epoxy exhibited considerable ductility even at -60^{o}C, well below its glass transition temperature T_g of 68^{o}C

The MDG$_c$ CZM should be considered to be a simple, phenomenological model that produces a mode-dependent toughness similar to that observed in interfacial fracture tests. Its interpretation in terms of a mode I separation process (e.g., at the tip of a blunted crack) coupled with additional dissipation due to shear yielding is meant to be suggestive and there is no expectation that this model provides a detailed description of the local crack-tip yielding. The intent is for the MDG$_c$ CZM to be used in analyses where the bulk material response is limited to small strains with essentially all the crack-tip energy dissipation directly incorporated into the MDG$_c$ CZM. Note that the current effort differs from other work that aims to perform a more detailed analysis that includes the large-strain plastic deformation in the bulk materials and resolves the local, nanometer-scale deformations (Swadener and Liechti 1998).

Figure 5-3 illustrates the two elements of the MDG$_c$ CZM. The plane strain version of this model is discussed first. Normal separation is defined by a mode I only version of what is now commonly referred to as a cohesive zone model (Barenblatt 1962; Needleman 1987; Tvergaard and Hutchinson 1992). The associated traction-separation (*T-U*) relationship defines how normal traction σ depends on normal interfacial separation δ_n (Fig. 5-3a). This relationship holds when $\delta_n \geq 0$, otherwise normal interpenetration is penalized by applying a prescribed multiple of the initial loading stiffness $k=\sigma^*/(\lambda_1 \delta_{nc})$. The two key parameters defining this *T-U* relationship are the interfacial strength σ^* and the intrinsic mode I work of separation/unit area of interface Γ. This study uses a trapezoidal *T-U* relationship where λ_1, λ_2 and the requirement that the traction vanishes when δ_n equals δ_{nc} define its shape. The trapezoidal *T-U* relationship was chosen for its simplicity and other forms could be used if there were a compelling reason to do so. The initial loading is defined by λ_1, while final stress decay is defined by λ_2,. For a trapezoidal *T-U* relationship, Γ, which equals the area under the *T-U* curve, has a value of $\Gamma=\frac{1}{2}\sigma^*\delta_{nc}[1+\lambda_2-\lambda_1]$. If unloading occurs prior to final separation, elastic unloading is assumed with an unloading stiffness equal to the initial *T-U* loading stiffness *k*.

The second element of the MDG$_c$ CZM defines perfectly plastic shear yielding (Fig 5-3b). The yield strength is τ^* and plastic slip is associated with the tangential displacement jump δ_t. The initial loading stiffness k was taken to be the same as used for normal separation. Here it is assumed that shear yielding only occurs prior to mode I softening (i.e., when $\delta_n < \lambda_1 \delta_{nc}$). Accordingly, shear stress is set to zero once $\delta_n > \lambda_1 \delta_{nc}$. The intent is to model interfacial crack growth where failure is associated with normal separation in the presence of interfacial shear. When there is interfacial compression, the interface can slip, but there is no limit to the extent of slip (i.e., shear cracking under interfacial compression is not modeled). The key parameter defining interfacial slip is the yield strength τ^*.

In this study, the initial stiffness k of the *T-U* model was chosen so that it was roughly equal to (or slightly greater than) the stiffness of adjoining elements, E_u/Δ, where E_u is the uniaxial strain modulus of the more compliant of the two adjoining bulk materials and Δ is the characteristic length of interfacial elements. This stiffness is not meant to model interface compliance. Rather, this stiffness can be thought of as a penalty that ties the adjoining interfacial materials together so as to prevent normal separation (i.e., the interface is intact when $\delta_n \leq \lambda_1 \delta_{nc}$ and begins to separate when $\delta_n > \lambda_1 \delta_{nc}$). With this interpretation, shear yielding occurs only in the region where the interface is intact and has not begun to separate (i.e., when $\delta_n < \lambda_1 \delta_{nc}$). As the cohesive zone develops and its length increases, interfacial shear is released whenever a previously intact portion of the interface begins to separate. It was anticipated that an abrupt reduction in interfacial shear might prove troublesome for the solver in these implicit quasistatic finite element calculations. Therefore, a capability for controlling the rapidity with which the shear is released was implemented by introducing a shear unloading stiffness k_u (controlled by λ_3, see Fig. 5-3b). Although this capability is potentially useful, it was not essential for the analyses reported herein. Finally, recall that the initial loading stiffness in shear was chosen to be the same as used for normal separation (Fig. 5-3b). As with normal separation, this initial stiffness can be thought of as a penalty that ties the adjoining interfacial materials together. Here it prevents relative tangential motion prior to plastic-slip.

The plane strain version of the MDG$_c$ CZM can generalize to 3-D by including anti-plane mode III slip δ_u in addition to the in-plane mode II slip δ_t by defining an effective shear stress τ_e and an effective slip rate $\dot{\delta}_e$ where

$$\tau_e = \left(\tau_t^2 + \tau_u^2\right)^{1/2} \text{ and } \dot{\delta}_e = \left(\dot{\delta}_t^2 + \dot{\delta}_u^2\right)^{1/2} . \quad (5\text{-}2)$$

$$\text{When } \left|\tau_e\right| < \tau^* \qquad \dot{\tau}_t = k\dot{\delta}_t \text{ and } \dot{\tau}_u = k\dot{\delta}_u . \quad (5\text{-}3)$$

$$\text{When } \left|\tau_e\right| = \tau^* \qquad \tau_t = \frac{\dot{\delta}_t}{\dot{\delta}_e}\tau^* \text{ and } \tau_u = \frac{\dot{\delta}_u}{\dot{\delta}_e}\tau^* \cdot \quad (5\text{-}4)$$

The MDG$_c$ CZM was implemented within the cohesive surface element framework available in Sandia National Laboratories' Sierra/SolidMechanics implicit quasistatics finite element code (Thomas 2011). This code implements cohesive surface elements (CSEs) within the context of large displacements where the CSE reference plane is defined by the average position of its upper and lower nodes. Sierra/SolidMechanics was used to generate all the finite element results reported in the present study.

5.3 Illustrative problem that illustrates nature of MDG$_c$ predictions

The plane strain problem of crack growth along the interface of a thin elastic layer sandwiched between rigid grips was analyzed (Fig. 5-4). This geometry, which models a thin adhesive bond with a long interfacial edge crack, is similar to that which has been used to measure the dependence of interfacial toughness on crack-tip mode-mixity (Swadener and Liechti 1998). The model geometry was chosen so as to closely approximate an infinitely long layer with a semi-infinite interfacial crack. Specifically, the layer length L equals $18h$ while the crack length a equals $6h$, where h is the height of the layer. The layer is loaded by applying uniform edge-normal and edge-tangential displacements to the upper rigid material while the bottom rigid material is fixed. The ratio of the normal-to-tangential edge displacements is held constant as the specimen is loaded. Test calculations showed that the layer is sufficiently long so as to generate a large uniformly stressed region in the central portion of the ligament with stress levels equal to those in an infinitely long layer. The finite element model geometry has a refined mesh in the region that surrounds the initial crack tip and cohesive surface elements were inserted along the interface in this refined region. In this region, the normalized characteristic element size Δ/h was typically in the range of 0.00125 to 0.0025 (the smaller cohesive zone elements were used when the choice of problem parameters generated a relatively small cohesive zone).

The interface's effective toughness Γ_e is defined as the value of the energy release rate when the interfacial crack first begins to propagate (i.e., when the maximum opening first equals δ_{nc}). This is calculated using the well-known (and easily derived via a J-integral evaluation) analytical energy release rate calibration for an edge-cracked elastic layer held between rigid grips,

$$\Gamma_e = \frac{h}{2E_u}(\overline{\sigma}^c{}_{yy})^2 + \frac{h}{2G}(\overline{\sigma}^c{}_{xy})^2 \qquad \text{(5-5)}$$

where $\overline{\sigma}^c{}_{yy}$ and $\overline{\sigma}^c{}_{xy}$ are the calculated critical values of the normal and shear stress in the uniformly stressed ligament when the crack begins to propagate, E is Young's modulus, ν is Poisson's ratio, $E_u = (1\text{-}\nu)\, E\, /((1+\nu)(1\text{-}2\nu))$ is the uniaxial strain modulus, and G is the shear modulus. In order to provide a formal connection to the crack-tip mode-mixity as defined in a linear elastic fracture mechanics solutions for an interface crack, an applied mode-mixity ψ_a is defined as

$$\psi_a \equiv \tan^{-1}(2\overline{\sigma}^c{}_{xy} / \overline{\sigma}^c{}_{yy}) \ . \qquad \text{(5-6)}$$

The crack-tip mode-mixity for a long interfacial crack in an elastic, semi-infinite bimaterial layer held between rigid grips and with one material rigid (i.e., the same problem as analyzed here, but without cohesive zone elements) can be expressed as (Hutchinson and Suo 1992)

$$\psi_{r=l_o} = \gamma + \omega + \varepsilon \ln(l_o / h) \qquad \text{(5-7)}$$

where ψ is evaluated at a reference length l_o. When the upper material is rigid and the lower elastic material has a Poisson's ratio of 1/3, the parameters ε and ω equal -0.081and -17^o, respectively, and $\gamma = \psi_a$ (as defined by Eq. 5-6) for plane strain. The choice of the reference length is arbitrary, but is often chosen as some fixed material length scale. If l_o/h=0.0025 (i.e., l_o is equal to characteristic length of a typical cohesive zone element) then $\omega + \varepsilon \ln(l_o / h) = 11^o$. It is important to note, however, that the linear elastic fracture mechanics solution is applicable only when the lengths of the cohesive zone and the yield zone are both small relative to the region dominated by the stress singularity (i.e., when there is "small-scale yielding").

The effective interfacial toughness depends on geometric parameters as well as interface and bulk material properties. This dependency can be expressed in terms of nondimensional parameters. The parameters that define the edge-cracked layer problem include elastic layer properties E and ν, interfacial properties σ^*, τ^*, Γ, λ_1, λ_2, and λ_3, elastic layer height h, and the critical ligament stresses when the crack begins to propagate $\bar{\sigma}^c{}_{yy}$ and $\bar{\sigma}^c{}_{xy}$ (note that both Γ_e and ψ_a are related to these stresses through Eqs. 5-5 and 5-6, respectively). The nondimensional parameters can be expressed in terms of Γ and σ^* (other choices are possible; this is simply a convenient choice). With this choice, the effective toughness can be expressed as

$$\Gamma_e / \Gamma = f\left(\psi_a, \frac{\sigma^*}{E}, \frac{\tau^*}{\sigma^*}, \frac{\Gamma}{\sigma^* h}, \nu, \lambda_1, \lambda_2, \lambda_3\right). \tag{5-8}$$

A series of calculations were performed where the applied mode-mixity was varied over a wide range of positive and negative values. Results presented here are for a configuration with σ^*/E=0.01, τ^*/σ^*=1.0, $\Gamma/(\sigma^* h)$=1e-4, and ν=1/3 (the *T-U* shape parameters were set to λ_1=0.1 and λ_2=0.9, while λ_3 was typically set to 0.01). For this choice of parameters, the cohesive surface elements have a characteristic length/critical normal separation Δ/δ_{nc}~10-20. This is consistent with the idea that a phenomenological cohesive zone model (e.g., MDG$_c$ CZM) incorporates behavior that obviates the need to use a highly refined crack-tip mesh to resolve details within the process zone (Tvergaard and Hutchinson 1993). Results for other parameter choices that explore how the solution depends on the most important of the nondimensional parameters identified above are presented elsewhere (Reedy and Emery 2014).

Figure 5-5 shows that the effective toughness (normalized by Γ) displays a strong dependence on applied mode-mixity with the effective toughness increasing rapidly with $|\psi_a|$. When ψ_a=+72^o, Γ_e/Γ=25. When ψ_a=-84^o, Γ_e/Γ=20. There is also a clear asymmetry with respect to ψ_a. When ψ_a=+63, Γ_e/Γ=11.9 When ψ_a=-63^o, Γ_e/Γ=2.6. Energy dissipation by interfacial shear yielding and slip generates the observed dependence of Γ_e on ψ_a since it is the only energy dissipation mechanism that depends on crack-tip shear. The length of the plastic slip zone L_s (defined as the region where interfacial shear stress equals τ^*) vanishes when -27< ψ_a< 0. Conversely, L_s can become a sizable fraction of h as $|\psi_a|$ increases. Note that the length of the cohesive zone (defined as the region where interfacial normal stress equals σ^*) is relatively insensitive to ψ_a and is less than 0.01h.

The source of the asymmetry can be illustrated by examining the special case where only positive or negative tangential edge displacement is applied (i.e., the normal edge displacement equals zero and $\psi_a = \pm\infty$). Figure 5-6 plots the normal traction T_n / σ^* in the cohesive surface element that is next to the initial crack tip (at the closest integration point) versus the applied shear $\bar{\sigma}_{xy}$ (normalized by the layer shear modulus G). When $\psi_a = +\infty$, $T_n < 0$, consequently an applied normal edge displacement must overcome this interfacial compression before it can generate tension to open the interface. When $\psi_a = -\infty$, $T_n > 0$. In this case an applied normal edge displacement only needs to augment the tension already induced by the shear loading to open the interface. Consequently, there is an indirect coupling between interfacial shear and normal opening. Interestingly, direct experimental observations of crack-tip opening/closing in a bimaterial test specimen showed the same sort of dependence on the direction of the applied tangential edge-loading (Liechti and Chai 1992).

A limited number of results aimed at assessing the accuracy of the MDG$_c$ cohesive zone (CZ) finite element calculations are reported in Table 5-1. First, a consistency check was performed by comparing the energy release rate/unit area at the initiation of crack growth Γ_e (as determined by Eq. 5-5 using the calculated critical values of the normal and shear stress in the uniformly stressed ligament) with the calculated energy dissipation/unit area. The energy dissipation is determined by summing 1) the energy associated with the intrinsic mode I work of separation/unit area of interface Γ and 2) the energy dissipated by shear yielding/unit area, which equals $\sim\tau^*|\delta_s|$, where δ_s is the maximum slip found at the tip of the cohesive zone (see Fig 5-3b). The ratio of these two quantities ranged from 0.94 to 1.01 with an average value of 0.98; a value close to the expected value of one (some of the deviation is thought to be due to discretization errors when estimating δ_s from the calculated results). Table 5-1 presents results that show only a modest change in Γ_e/Γ when a coarser mesh is used and insensitivity to the choice of λ_3 (which controls the rapidity of shear unloading, see Fig. 5-3b). As an aside, when $\psi_a < 0$, relatively small drops in interfacial normal stress σ occurred when the interfacial shear stress was removed as the cohesive zone advanced (less than $\sim 0.05\sigma^*$). This elastic unloading was recovered with additional edge-normal applied displacement. The inclusion of λ_3 in the MDG$_c$ CZM provides a way to slow down this shear unloading step. This worked as expected, but for suitable solution tolerances, convergence could still be attained with λ_3 set to ~0. As a further check, an explicit dynamic finite element analysis was performed for one of the cases where a transient decrease in normal stress occurred to examine of the possible role of dynamic unloading. The calculated load at crack growth was essentially identical (within 0.3%).

5.4 Validation of MDG$_c$ predictions

The elastic bond with a long interfacial edge-crack geometry analyzed in section 5.3 is of the same the type as used by other researches to measure the interfacial toughness of a glass/epoxy interface (Swadener and Liechti 1998). This allows a comparison of results of an analysis that uses the MDG_c CZM with experimental data. In the Swadener and Liechti study (referred to as the SL study) an epoxy layer is sandwiched between relatively stiff aluminum and glass adherends that are subjected to bond-normal and bond-tangential edge displacements. The epoxy layer's E is reported be two GPa, while the layer thickness h falls within the range of 0.13 to 0.4 mm, and the intrinsic work of separation Γ was determined to be in the range of 1 to 2 J/m^2. Various combinations of applied edge displacements propagated a long interfacial edge crack along the glass/epoxy interface. Figure 5-7 compares SL experimental results with calculated Γ_e vs. ψ_a relationships. The nondimensional MDG_c CZM parameters used in these calculations are based on the reported SL test configuration (i.e., E = 2 GPa, h=0.25 mm, and Γ=1.5 J/m^2). Specifically, σ^*/E,=0.02, $\Gamma/(h\sigma^*)$ =1.5e-4, and τ^*/σ^* = 0.5. Note that the SL results are reported in terms of crack-tip mode-mixity and the epoxy layer is considered to be "material one" in the definition of the bimaterial constant ε. To enable a direct comparison with the calculated Γ_e/Γ vs. ψ_a relationships, the SL crack-tip mode mixity is converted to applied mode mixity ψ_a via Eq. 5-7 (also reverse the sign of ψ_a to make the epoxy layer "material 2"). The SL toughness data was also normalized by the apparent intrinsic work of separation (i.e., by the minimum of the measured Γ_e vs. ψ relationship) to define the experimental Γ_e/Γ. The asymmetry in the calculated Γ_e/Γ vs. ψ_a relationship is similar to that measured. Figure 5-7 demonstrates that a finite element analysis that uses the MDG_c CZM is capable of generating the same type of mode-mixity dependent toughness as observed experimentally for a glass/epoxy interface.

In addition to the higher level toughness versus mode-mixity data, the SL study also reports local crack-tip displacement data (see Fig. 5 in Swadener and Liechti, 1998). A few data points that represent the general trend in their normal crack-tip opening displacement versus distance from the crack tip data are plotted in Fig. 5-8 (note that the SL plot contains a multitude of data points with some natural variability). This data has been normalized by the bond thickness h. Also shown in Fig. 5-8 are the calculated normal crack opening displacements for ψ_a =0 and using the same nondimensional MDG_c CZM parameters that matched the toughness data in Fig. 5-7. In the analysis, the crack-tip is defined as the position where the interfacial normal stress σ first equals the interfacial strength σ^*. Note that within the cohesive zone, elasticity theory results indicate that the crack-tip displacements should generate a cusp-like opening (Barenblatt 1962). For this reason, comparison between the analysis and experiment should be confined to distances beyond the end of the cohesive zone (the end of the cohesive zone is indicated in Fig. 5-8). There is good agreement between analysis and experiment. This demonstrates that when the MDG_c CZM calculation generates a good match to Γ_e/Γ vs. ψ_a data, it also generates local crack-tip deformations that are in reasonable agreement with experimental results. This consistency in the predictions is encouraging.

It should be emphasized that the calculated shape of the Γ_e/Γ vs. ψ_a relationship is not predefined, but instead is the outcome of applying the MDG_c CZM to the particular problem geometry of interest. As such, one might expect that calculated Γ_e/Γ vs. ψ_a relationships may differ for different specimen geometries unless small scale yielding-like conditions apply (i.e., unless the slip zone is embedded within the crack-tip singular field over the full range of mode-mixity).

The results presented above provide some guidance on how to define the three principal nondimensional MDG$_c$ CZM parameters τ^*/σ^*, σ^*/E, and $\Gamma/(h\sigma^*)$. In these simulations the MDG$_c$ CZM incorporates all energy dissipation mechanisms, and the bulk materials were modeled as linear elastic. The value of the intrinsic work of separation Γ reflects the fundamental energy dissipation mechanisms at low applied mode-mixity and is assumed to be a known (or estimable) quantity. The bond's thickness h and Young's modulus E are also assumed to be known quantities. In this study the nondimensional parameter σ^*/E was typically chosen to be in the range of 0.005 to 0.02 to avoid large crack-tip strains that would necessitate the use of a highly refined crack-tip mesh. This is consistent with the idea that the phenomenological MDG$_c$ CZM incorporates behavior that obviates the need to resolve details such as crack-tip blunting. Once σ^*/E is set, the value of $\Gamma/(h\sigma^*)$ is also set (since E, h, and Γ are known). Knowledge of the effective toughness at a relative high mode-mixity is also desirable since the remaining parameter τ^*/σ^*, can then be chosen so as to generate a horizontal offset in the Γ_e/Γ vs. ψ_a relationship that best fits the high mode-mixity toughness data (Reedy and Emery 2014). Without such data, a choice of τ^*/σ^* =0.5 is recommended. This approach for choosing MDG$_c$ model parameters should only be considered an initial suggestion based on limited experience and it strictly applies only to the edge-cracked elastic layer geometry considered in this study.

Table 5-1. Selected results assessing the accuracy of the MDG$_c$ CZM finite element calculations.

Ψ_a (degree)	Δ/h	λ_1	λ_3	Γ_e/Γ
-63	0.00250	0.10	0.001	2.6
-63	0.00125	0.10	0.001	2.5
-63	0.00250	0.10	0.300	2.6
63	0.00250	0.10	0.001	11.9
63	0.00125	0.10	0.001	11.8
63	0.00250	0.10	0.500	11.9

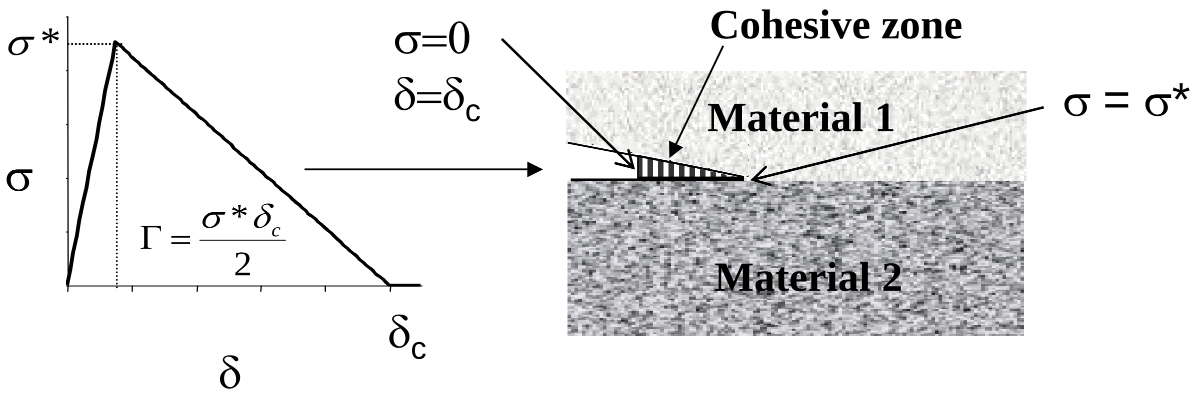

Figure 5-1. Illustration showing traction-separation relationship and associated cohesive zone.

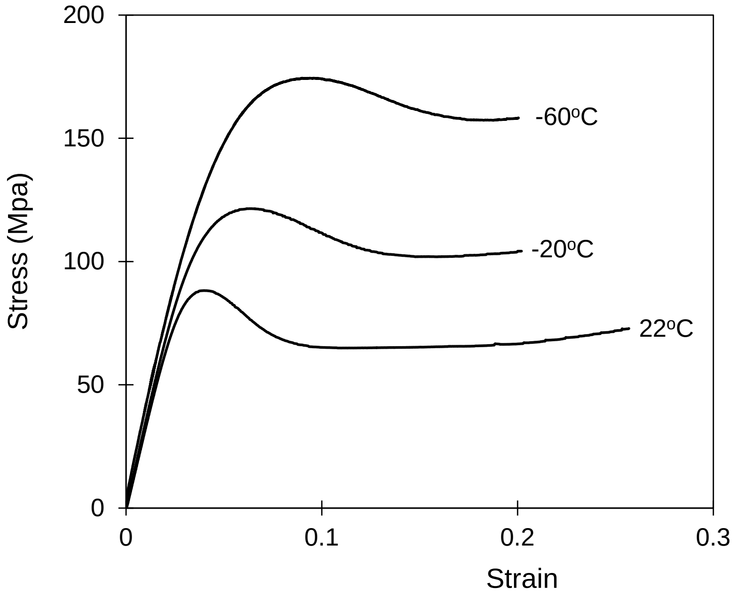

Figure 5-2. Epoxy can exhibit ductile-like response in compression (Epon 828/T403, 100:43 pbw, cured 24 hr. at 50°C followed by 24 hr. at 40°C). Tested at a nominal strain rate of 0.00027/s.

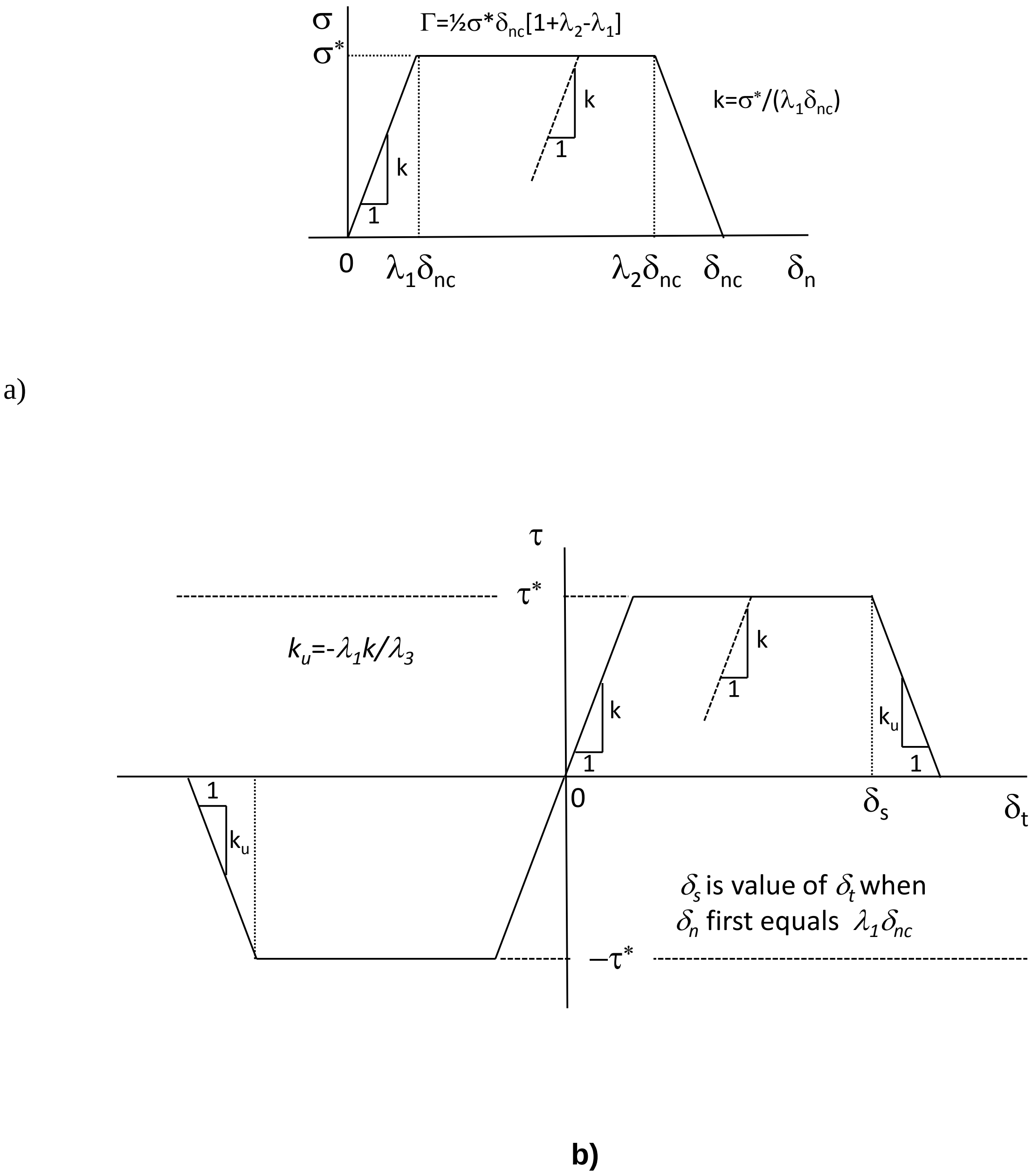

Figure 5-3. Plane strain cohesive zone model a) traction-separation relationship for mode I separation, and b) model for interfacial shear yielding when $\delta_n < \lambda_1 \delta_{nc}$ (i.e., prior to mode I softening).

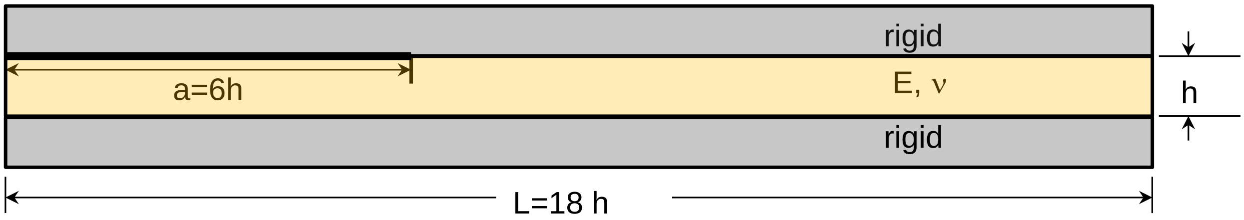

Figure 5-4. A long, edge-cracked elastic layer sandwiched between rigid adherends with edge-normal and edge-tangential displacements applied to the upper rigid material while the lower rigid material is fixed.

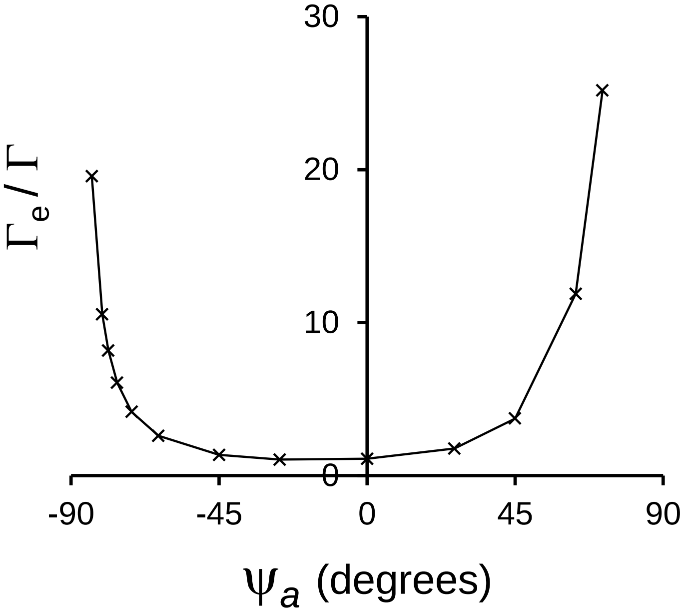

Figure 5-5. Effective toughness Γ_e (normalized by Γ) versus the applied mode mixity ψ_a.

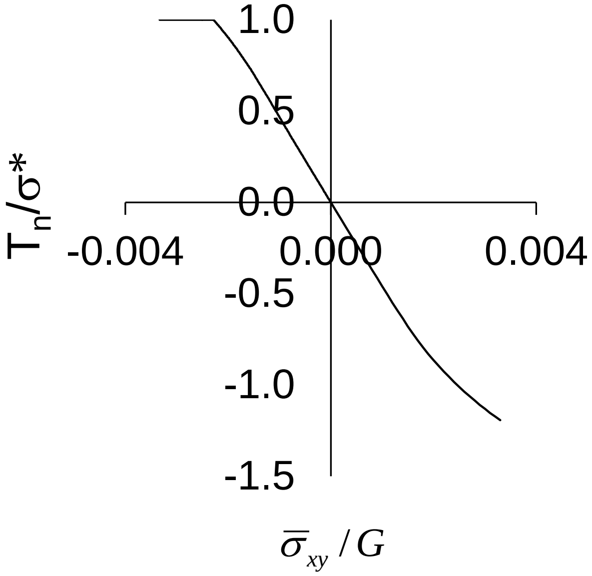

Figure 5-6. Normal traction T_n in the cohesive surface element that is next to the initial crack tip vs. the applied shear $\bar{\sigma}_{xy}$ when the edge-normal displacement is zero (i.e., $\psi_a=\pm\infty$).

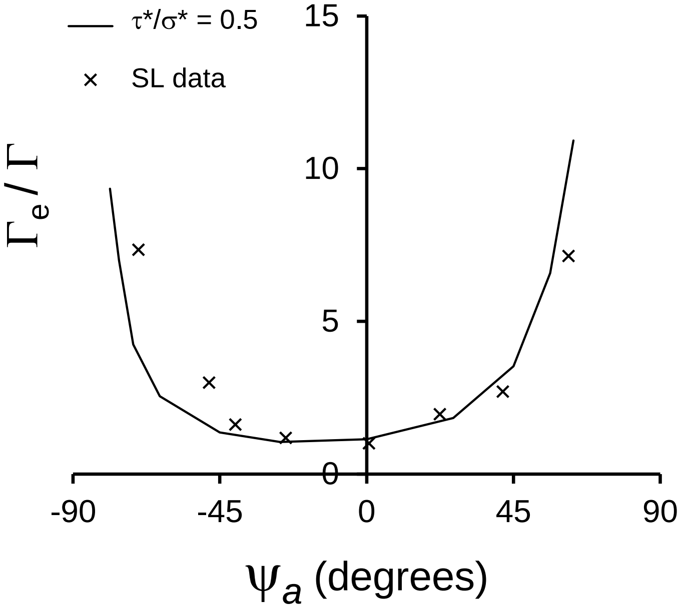

Figure 5-7. Comparison of finite element analysis predictions that use the MDG_c CZM with experimental interfacial toughness data published by Swadener and Liechti (SL).

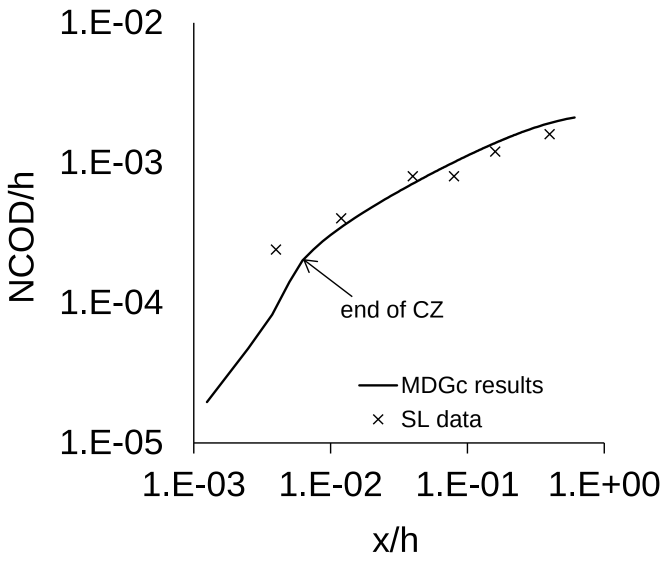

Figure 5-8. Comparison of finite element analysis predictions that use the MDG$_c$ CZM with experimental normal crack opening displacement data (NCOD) published by Swadener and Liechti (SL).

6. ILLUSTRATE CALCULATIONS THAT USE NLVE SPEC ADHESIVE MODEL AND MDG$_C$ CZM

6.1 Tensile-loaded, adhesively bonded butt joint with an interfacial edge crack

A tensile-loaded, adhesively bonded butt joint is analyzed (Fig. 6-1). This type of joint is commonly used to evaluate adhesives and is also a relatively simple geometry to analyze. In particular, the case where there is a pre-existing edge crack was considered. The finite element model geometry has a refined mesh in the region that surrounds the initial crack tip. Cohesive surface elements with a normalized characteristic element length Δ/h=0.005are inserted along the interface in this refined region. As a further simplification, this plane strain finite element analysis assumes that the adhesive layer is sandwiched between rigid adherends and that layer is relatively thin so that the stress in the interior of the joint is unaffected by the stress-free edge. Since symmetry boundary conditions are applied, only one half of the layer is modeled and L/h >18 (where L is the half-width of the joint). Test calculations showed that the stress state at the center of the layer is uniform for this L/h ratio. The adhesive layer is modeled as either a linear elastic material or as a nonlinear viscoelastic material. The joint is loaded by 1) first applying a uniform temperature change to induce residual stress within the bond (bottom adherend fixed while upper adherend translates in upwards as dictated by the thermal expansion), and then 2) applying a tensile load (bottom adherend fixed, top adherend uniformly displaced upwards). Results for an initial short crack (a/h = 0.1) are contrasted with those for a long crack (a/h=6), where bond thickness h equals 1 mm. The results are also compared to results of a linear elastic fracture mechanics (LEFM) analysis.

As an aside, one could perform a cohesive zone model-based fracture analysis of an adhesively bonded butt joint without inserting a pre-existing crack by simply inserting cohesive surface elements along the interface starting at the interface corner (i.e., from the point where the interface intersects the stress-free edge). However, a recent study has shown that this approach is problematic (Reedy 2014). In that study there was no preexisting crack, and the predicted strength of a rigid adherend, adhesively bonded butt joint was found to depend on the shape of the *T-U* relationship used in the CZ fracture analysis. In some sense, the CZ can be considered to be the “initial flaw” when there is no preexisting crack and, consequently, the shape of the *T-U* relationship matters since it controls the length of the CZ as well as the magnitude and distribution of CZ tractions. Furthermore, it was shown that in an analysis where there was no preexisting crack, a CZM can use any number of *T-U* relationships to generate the same joint strength. Consequently, identifying a *T-U* relationship that predicts the measured joint failure load does not mean that that *T-U* relationship is a material-like property since other *T-U* relationships could also generate the same failure load.

Linear elastic fracture mechanics analysis

A linear elastic interfacial fracture mechanics analysis was performed to provide results to compare with those determined by a finite element analysis that treats the epoxy as a NLVE material and simulates interfacial fracture using the MDG$_c$ CZM. The form of the singular crack-tip stress field for a crack lying on the interface between two dissimilar, linear-elastic, isotropic materials is well known (Rice 1988; Hutchinson and Suo 1992). This asymptotic stress field is characterized by a complex stress intensity factor $K=K_1+iK_2$. In the present work K-values were determined for interfacial cracks of varying length using crack-flank displacements as calculated by a finite element analysis (FEA) that uses a highly refined and focused crack-tip mesh (Matos, McMeeking et al. 1989). Calculated results are for a thin elastic layer sandwiched between rigid adherends (plane strain).

When the layer is subjected to a uniform shrinkage strain ε_o^*, the solution for *K* can be expressed as

$$\frac{(K_1 + iK_2)}{\hat{\sigma}\sqrt{h}} = f_{1\varepsilon_o^*}(a/h,\nu) + if_{2\varepsilon_o^*}(a/h,\nu) \tag{6-1}$$
$$\text{where } \hat{\sigma} = -\frac{E\varepsilon_o^*}{1-\nu} \text{ and } \varepsilon_o^* = \alpha_b \Delta T$$

where α_b is the adhesive's coefficient of thermal expansion and ΔT a uniform temperature change. Selected values of $f_{1\varepsilon_o^*}(a/h,\nu)$ and $f_{2\varepsilon_o^*}(a/h,\nu)$ are presented in Table 6-1. Here *E* is the layer's Young's modulus and ν is its Poisson's ratio.

When the layer is subjected to a bond-normal tensile loading as generated by a uniform edge displacement *U**, the *K* solution can be expressed as

$$\frac{(K_1 + iK_2)}{\hat{\sigma}\sqrt{h}} = f_{1\sigma_n^*}(a/h,\nu) + if_{2\sigma_n^*}(a/h,\nu) \tag{6-2}$$
$$\text{where } \hat{\sigma} = \frac{\nu}{1-\nu}\sigma_n^* \text{ and } \sigma_n^* = E_U U^*/h$$

where $E_u=(1-\nu)E/((1+\nu)(1-2\nu))$ is the uniaxial strain modulus. Selected values of $f_{1\sigma_n^*}(a/h,\nu)$ and $f_{2\sigma_n^*}(a/h,\nu)$ are presented in Table 6-2. Note that when the upper adherend is rigid (i.e., material 1 is the rigid adherend, material 2 is the elastic layer, and the interfacial crack lies between materials 1 and 2), the elastic mismatch parameters α and β (Dundurs 1969) and the bimaterial constant ε are given by

$$\alpha = 1,\ \beta = (1-2\nu)/(2(1-\nu)),\ \text{and } \varepsilon = -\ln(3-4\nu)/(2\pi) \tag{6-3}$$

Furthermore, the energy release rate *G* for crack advance along the interface is related to the complex interfacial stress intensity factor by

$$G = \frac{(1-\beta^2)}{E^*}|K|^2 \text{ where } |K|^2 = K_1^{\,2} + K_2^{\,2} \text{ and } E^* = \frac{2E}{(1-\nu^2)} \tag{6-4}$$

The solutions presented above (i.e., Eqs. 6-1 and 6-2) can be superimposed to determine the complex stress intensity factor for a bond that is first cooled and then subjected to a tensile load. Consequently, one can use these results to predict the joint tensile stress σ_t^* at crack advance σ_f (i.e., joint strength) for a specified uniform shrinkage ε_o^*, crack length, and interfacial toughness Γ (i.e., failure occurs when $G=\Gamma$).

Finite element analysis using the MDG$_c$ CZM

In these calculations the adhesive layer was modeled as either a linear elastic material or as a NLVE material (using the SPEC model for EPON 828/T403 epoxy; see section 3.1). The linear elastic material model was chosen so as to be consistent with elastic properties that the NLVE analysis would predict. Table 6-3 lists the elastic properties used in those simulations that assumed linear elastic bond. These properties are based on the results presented in Table 3-3 (i.e., from values computed in one-element simulations that used the EPON 828/T403 NLVE material model). The intent is to choose elastic properties that are consistent with the glassy properties associated with the particular temperature and loading rates used in the NLVE analysis to enable a comparison between elastic and NLVE adhesive model results. The coefficient of thermal expansion of the bond α_b was determined by performing a one-element uniaxial strain calculation (i.e., zero transverse strain). A linear elastic uniaxial strain analysis that uses the inferred effective elastic properties E, ν, and α_b, will generate the same transverse stress as determined by a one-element NLVE uniaxial strain calculation when a reference temperature 90^{o}C is used. Note that in a rigid adherend butt joint, the center of the bond (away from the stress-free edge) is loaded uniaxial strain.

The parameters that define the MDG$_c$ CZM were selected as follows. The interfacial strength σ^* was set to equal 60 MPa (roughly 2% of the Young's modulus E) so as to avoid large crack-tip strains. The interfacial yield strength τ^* was set equal to roughly 80% of the epoxy's shear yield strength with the selected values listed in Table 6-3 (i.e., $\tau^*{\sim}0.8\sigma_y/3^{1/2}$, where σ_y values are listed in Table 3-3). A value that is somewhat less than that of the epoxy's shear yield strength was chosen so as to avoid the possibility of extensive, yield-like behavior in the bulk material. This is consistent with the idea that the cohesive zone model incorporates all the crack-tip dissipation generated within the process zone. Calculations were performed for two values of Γ, the intrinsic work of separation/unit area of interface (25 J/m^2 or 50 J/m^2). Test calculations showed that these values generated predicted butt joint failure strengths that are in the range of measured values. The shape parameters λ_1, λ_2, and λ_3 were set equal to 0.05, 0.99, and 0.0001, respectively. Finally, note that the Sierra/SolidMechanics contact surface capability was used to ensure that crack flank surfaces do not interpenetrate during cooling (test calculations showed that such contact can occur during cooling step).

Results

Results for the short crack case (a/h=0.1) will be discussed first. Figure 6-2 plots the LEFM predictions for joint strength vs. the temperature to which the joint is cooled prior to mechanical loading. The analysis predicts that joint strength decreases as the temperature prior to mechanical loading decreases. Furthermore, for the lower toughness interface (Γ=25 J/m^2), the crack can grow just by cooling the joint. In contrast, a finite element analysis that uses the MDG$_c$ CZM predicts joint strength increases as test temperature decreases (Fig. 6-3). There is a ~20% increase in predicted joint strength as temperature is reduced from 25°C to -25°C for a fixed value of *Γ*. In these calculations, there is a small region of crack-flank contact immediately adjacent to the crack-tip. Consequently, the crack-tip is closed during the cooling step and the crack is subjected to a purely mode II sliding. Thus, unlike the LEFM analysis, the MDG$_c$ CZM predicts shear yielding and energy dissipation associated with shear yielding, but not failure during cooling (i.e., as discussed in section 5.2; the traction-separation relationship depends only on normal separation). Also note that modeling the adhesive bond as a linear elastic material introduces only a modest shift in the predicted joint strength relative to that predicted when the bond is modeled as a NLVE material (Fig. 6-3). The modest difference in predicted strength reflects the manifestation of viscoelastic response as the bond is cooled through its glass transition temperature until it becomes glassy (elastic). The bond response is essentially linear elastic during the mechanical load step (as well as during much of the cooling step). The results of the FEA that use the MDG$_c$ CZM are broadly consistent with observation in that the measured strength of an adhesively bonded butt joint increases as the temperature decreases (Table 2-1).

The results for a long crack (a/h=6.0) are discussed next. Figure 6-4 shows that LEFM and finite element analyses that use the MDG$_c$ CZM (with either the elastic or NLVE bond model) all predict essentially the same joint strength and this strength is nearly independent of the temperature at the end of the cooling step (for *Γ* fixed at 25 J/m^2). This is as expected. When crack is sufficiently long, the strain energy at the stress-free edge should be negligible and the residual stress is "locked in" since one side of bond remains attached to the rigid adherend (i.e., there is no contribution to the energy release rate as the long crack extends). The fact that residual stress in a thin-layer-sandwich does not drive crack growth has been previously noted by others (Hutchinson and Suo 1992). Furthermore, for a long crack, the crack is subjected to a primarily a mode I-like loading, so mode-mixity effects are minimized. Consequently one expects that the calculated joint strength should approach that predicted by the long-crack *G* calibration for bond-normal displacement where residual stress is ignored (see Eq. 5-5).

$$\sigma_f = \sqrt{2E_u \Gamma / h} \qquad (6\text{-}5)$$

where E_u is the uniaxial strain modulus. Figure 6-4 shows this to be the case (the long-crack G analysis prediction is ~ 4% lower; this reflects the fact that the strain energy density generated by cooling is relatively small, but does not vanish at the stress-free edge). The 7% increase in σ_f as the temperature decreases from 25°C to -25°C is associated with the corresponding increase in E_u.

Long-crack estimate of butt joint strength

A first cut estimate of the strength of adhesively bonded butt joints like those tested (Table 2-1) can be made using the long-crack estimate (Eq.6-5). Table 6-4 lists the values of the parameters used in the estimate as well as the estimated strength. The elastic properties correspond to those measured for the same Epon 828/T403 epoxy as used to fabricate the butt joints (100:43 pbw, cured 24 hr. at 23°C, followed by 3 hr. 50°C, followed by 15 hr at 80°C). The Young's modulus was assumed to increase by 20% as the joint is cooled from RT to -50°C (consistent with Fig. 3-10). Figure 2-1 shows that the measured interfacial toughness increases from 90 J/m^2 to 150 J/m^2

as the temperature is deceased from RT to -50^{o}C (i.e., Γ increases by ~ 67% as the test temperature as decreased). Based upon these parameters, the estimated joint strength increases from 34 MPa at RT to 48 MPa at -50^{o}C; a 40% increase. The measured butt joint strength was 27 MPa at RT and 38 MPa at -50^{o}C, also a 40% increase. The first cut, long-crack estimate for joint strength is ~ 25% too high. This is not surprising since the fracture surfaces indicate that crack growth is 3D in nature with initiation from a single point on the outer, bond periphery. The plane strain, long-crack idealization is clearly a gross simplification. Nevertheless, this result seems to suggest that the increase in joint strength with decreasing temperature may be largely attributable to the increase in interfacial toughness with decreasing temperature.

6.2 Buckle-driven growth of 1-D blister on a rigid substrate

MDGc CZM has also been used to analyze buckle-driven growth of a one-dimensional blister on a rigid substrate (Fig. 6-5). In this analysis the film is assumed to be linear elastic and there is an initial delamination of length $2b$. The film is subjected to an increasing compressive biaxial stress until it reaches a critical value σ_{oc} at which the buckled film (blister) begins to extend laterally. There is a closed form solution for the energy release rate for this problem (Hutchinson and Suo 1992), and this solution can be used to make a mode-mixity independent prediction (Fig. 6-6, analytic 1D blister solution for for ν=1/3, Γ/Eh=6.67e-5). Also shown on Figure 6-6 are finite element solutions that used either a mode-mixity independent CZM (Tvergaard and Hutchinson 1993) or the present MDGc CZM (for nondimensional MDGc CZ parameters σ^*/E=3.33e-3, τ^*/σ^*=1.0, $\Gamma/(\sigma^*h)$=0.02, ν=1/3). As expected, the Tvergaard and Hutchinson model (T-H CZM) agrees with the predictions based on the closed-from solution. On the other hand, the MDG$_c$ CZ fracture model generates results that differ significantly from that of the mode-mixity independent solutions. In these calculations the critical compressive biaxial stress increases rapidly with the length of the initial delamination. This suggests that buckles will not keep spreading once they begin to propagate. This prediction, which differs from one based on a mode-mixity independent toughness, is consistent with experiments that find that blisters have a characteristic finite width (Cordill, Bahr et al. 2007).

Table 6-1. LEFM solution for a rigid adherend butt joint with an interface edge crack for a uniform adhesive shrinkage (*ν*=0.42).

a/h	$f_{1\varepsilon_o^*}(a/h,\nu)=\frac{K_1}{\hat{\sigma}\sqrt{h}}$	$f_{2\varepsilon_o^*}(a/h,\nu)=\frac{K_2}{\hat{\sigma}\sqrt{h}}$
0.01	0.2334	-0.2332
0.1	-0.1606	-0.3103
0.5	-0.5877	-0.5757
1	-0.8056	-0.4253
10	-0.0010	-0.0002

Table 6-2. LEFM solution for a rigid adherend butt joint with an interface edge crack for a bond-normal tensile loading (*ν*=0.42).

a/h	$f_{1\sigma_n^*}(a/h,\nu)=\frac{K_1}{\hat{\sigma}\sqrt{h}}$	$f_{2\sigma_n^*}(a/h,\nu)=\frac{K_2}{\hat{\sigma}\sqrt{h}}$
0.01	0.4864	-0.2622
0.1	0.6165	-0.3092
0.5	0.7165	-0.4066
1	0.8109	-0.3882
10	0.8693	-0.3195

Table 6-3. Temperature-dependent properties used the adhesively bonded butt joint with interfacial edge crack calculations.

^{o}C	E (MPa)	ν	α (C^{-1})	τ^* (MPa)
25	2600	0.42	8.0E-05	40.0
0	2800	0.42	8.0E-05	50.0
-25	3000	0.42	8.0E-05	62.5

Table 6-4. Long-crack estimate of butt joint strength for a one mm-thick bond.

^{o}C	E (MPa)	ν^{a}	E_u (MPa)	Γ (J/m^2)^c	σ_f (MPa)
23 (RT)	3150^a	0.39	6280	90	34
-50	3780^b	0.39	7540	150	48

[a] measured Epon828/T403 RT *E* and ν (see section 2.1)

[b] estimated 20% increase in *E* as cool from RT to -50^{o}C (see Fig. 3-10)

[c] interpolated measured temperature-dependent Γ (see Fig. 2-1)

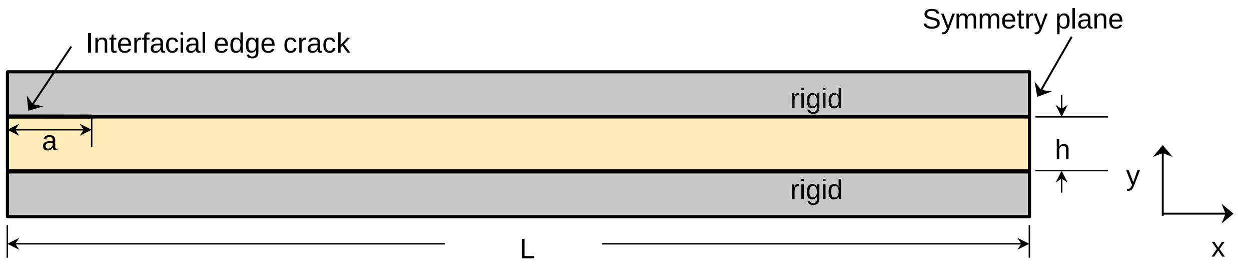

Figure 6-1. An edge-cracked layer sandwiched between rigid adherends with edge-normal displacements applied to the upper rigid material while the lower rigid material is fixed.

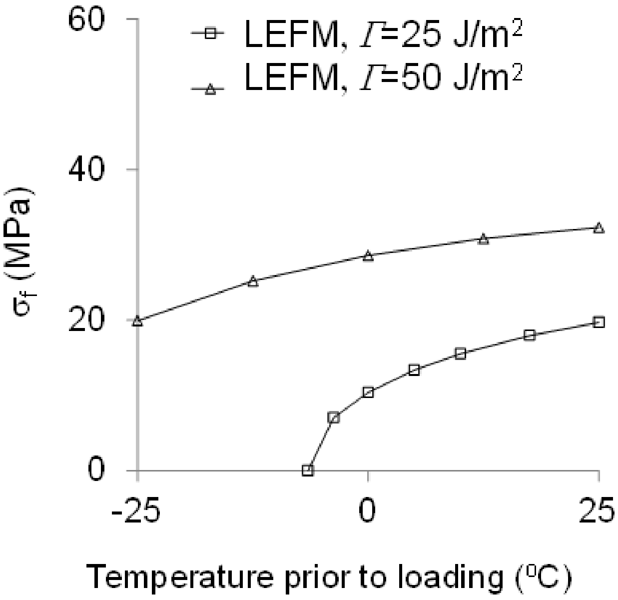

Figure 6-2.Predicted strength for an adhesively bonded butt joint with a short interfacial edge crack of length *a/h*=0.1 as determined by a LEFM analaysis

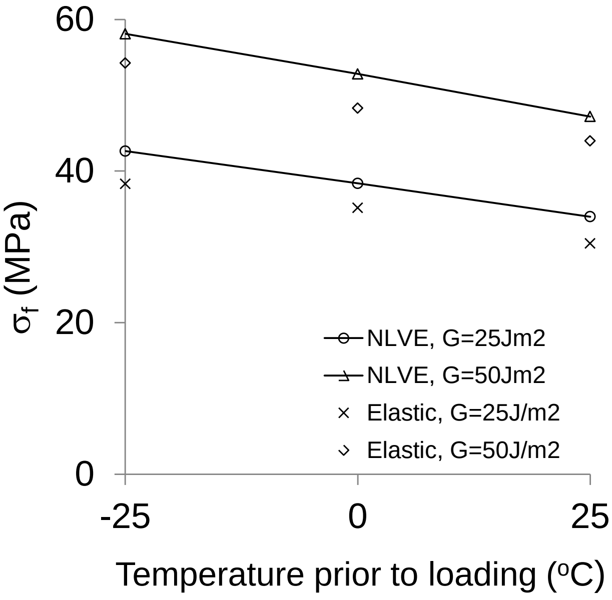

Figure 6-3. Predicted strength of an adhesively bonded butt joint with an interfacial edge crack of length *a/h*=0.1 as determined by a FEA that uses the MDG$_c$ CZM.

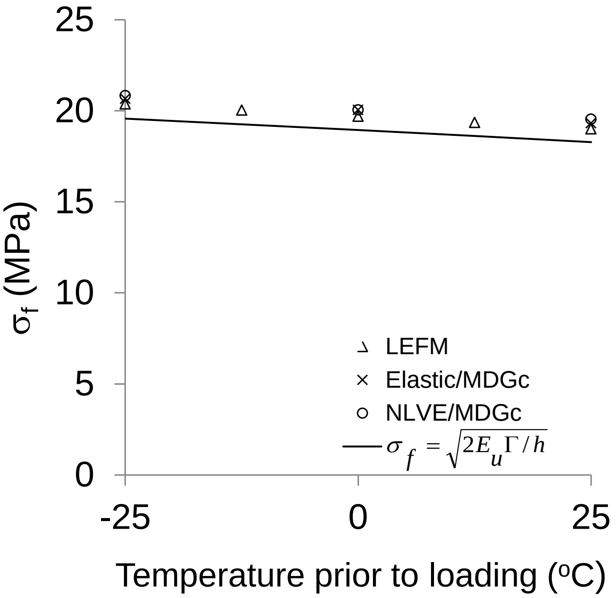

Figure 6-4. Predicted strength of an adhesively bonded butt joint with a long interfacial edge crack of length *a/h*=6.0 as determined by LEFM analysis and also a FEA that uses the MDG$_c$ CZM.

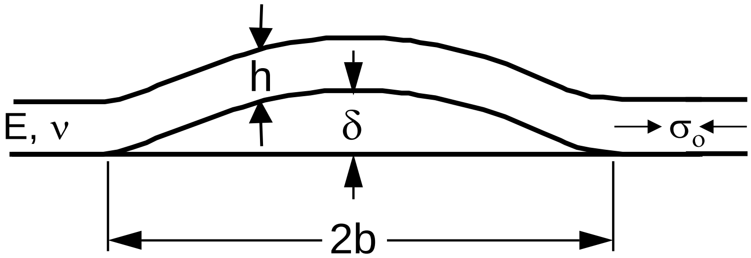

Figure 6-5. Buckle-driven growth of 1-D blister on a rigid substrate.

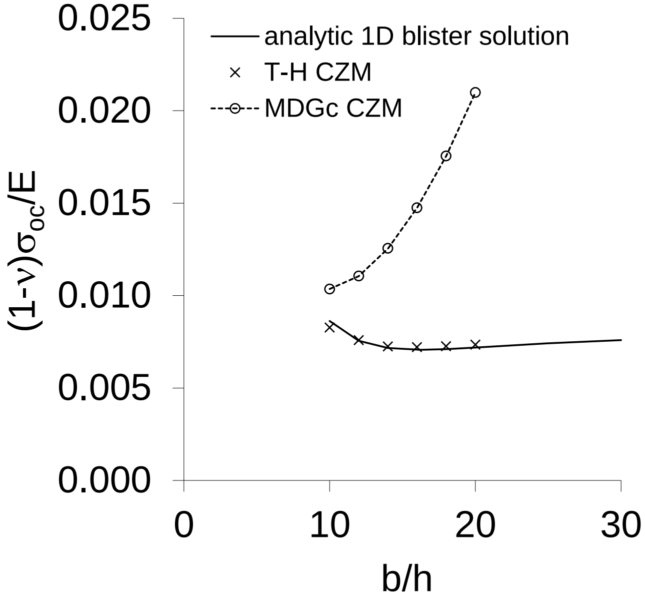

Figure 6-6. Comparison of the calculated critical misfit stress to propagate a one-dimensional blister that has an initial length of *b/h* (mode-mixity independent T-H CZM vs. mode-mixity dependent MDGc CZM).

7. MOLECULAR DYNAMICS SIMULATIONS OF ADHESIVELY BONDED BUTT JOINT

7.1 Introduction

The mechanics of polymer adhesives is intrinsically multiscale involving the bonding of one material to another at the molecular scale and the stresses applied at the macro scale (Kinloch 1987; Kendall 1994; Gay and Leibler 1999). Polymeric adhesives are the preferred bonding method for many applications, because they produce excellent interfacial bonds and dissipate energy on larger scales. In particular, epoxies are highly crosslinked polymer networks preferred in structural applications. Understanding the molecular mechanisms of fracture in such systems is a complex challenge of connecting molecular structure over multiple length scales with mechanical behavior.

Linear elasticity theory gives a connection between the local stress at a corner between the adhesive and the adherend and the thickness of the adhesive (Williams 1952; Timoshenko and Goodier 1970). This stress is singular of the form K $r^{-\delta}$ where K is the stress intensity factor and $\delta \geq 0$ is a function of the Poisson's ratio when the adherends are rigid (Williams 1952; Timoshenko and Goodier 1970)). Moreover, K increases with increasing thickness h of the adhesive as h^{δ}(Reedy 1990). This has important practical consequences as it indicates that flaws at corners are especially prone to failure. To understand the connection between the macroscopic stress and molecular scale deformations in polymer adhesives, systems with open surfaces and corners need to be analyzed.

To address the above issues, molecular dynamics (MD) simulations of a model epoxy system bonding together two solid surfaces with open sides and corners have been performed. The effect of system size on fracture for a model epoxy is examined and connections are made between the molecular scale interfacial dynamics with the system's stress-strain curves. Significant system size dependence of fracture initiation and failure is found. These results have significant implications on the nature of the underlying physical phenomena and in performing comparisons between simulation and experiments on epoxies.

Our previous simulations on coarse-grained, highly crosslinked polymer networks modeling epoxies calculated stress-strain behavior for the network between two parallel plates with periodic boundary conditions on the sides (Stevens 2001; Stevens 2001; Tsige, Lorenz et al. 2004). Unexpectedly, very large failure strains (>1.0) were found even though the network was highly crosslinked with very short strand lengths. In experiments on much larger epoxy adhesives, the failure strains are near 0.1 for tensile and are up to about 0.3 for compression (Morgan, Kong et al. 1984; Chen and Zhou 1998). The expectation was that the short strands in an epoxy could only be strained a small amount before bond breaking. The simulations found that the strands have a compact structure that requires a large strain to unfold and does so without stressing the bonds. Consequently, a long plateau regime in the stress-strain curves occurs while the strands are being unfolded and pulled taut. Because the strands are compact, the minimal path length through the network from one surface binding site to the another site on the opposite surface is greater than twice the plate separation (Stevens 2001) . Only at these large strains, do the strands become sufficiently taut and the stress increase ultimately causing bond breaking and failure. The failure strain in these systems without open sides did not vary significantly as a function of system size.

More recently there have been a range of simulations of epoxies (Li and Strachan 2015). Liu et al. have developed multiscale techniques for curing and construction of the network structure (Liu, Li et al. 2011). Atomistic models have been developed and mechanical properties such as the elastic moduli calculated (Wu and Xu 2006; Wu and Xu 2007; Varshney, Patnaik et al. 2008; Li, Medvedev et al. 2012; Yang, Gao et al. 2013; Li and Strachan 2015). The failure strains for the atomistic simulations of Yang et al. are also large at about 1.0 (Yang, Gao et al. 2013). Yang and Qu developed a coarse-grained model of an epoxy from atomistic simulations, which like our previous results gives very large failure strains (Yang and Qu 2014).

Local elastic moduli have been calculated for simpler systems and shown to be connected to critical deformations (Chikina and Gay 2000; Yoshimoto, Jain et al. 2004; Rottler 2009; Makke, Perez et al. 2011; Guan, Lu et al. 2013). The nucleation of cavities in an uncrosslinked polymer glass under tensile strain has been shown to be where the local elastic moduli are large (Makke, Perez et al. 2011). Simulations of simpler amorphous solids have found that classical nucleation theory can be used to describe cavitation and similar behavior has been seen in glassy polymers (Guan, Lu et al. 2013) . Given the similarities in the models, the cavitation that occurs in the epoxy tensile simulations during the long plateau of the stress-strain curve should have the same origin (Stevens 2001; Yang and Qu 2014). Calculation of the local stress in a corner has not been reported for polymers, but the rise of the corner stress with system size on the atomic scale has been seen in simulations of a crystal at very low temperatures (Vafek and Robbins 1999). To minimize the fluctuations in the local stress, the simulations had to be performed for crystals and at temperatures close to 0^{o}K. In polymeric systems, yielding typically occurs limiting the application of linear elasticity, but the concept of large stress in corners is expected to hold and is examined in this work.

7.2 Simulation Methods

The model of highly cross-linked polymer networks is the based on earlier work (Stevens 2001; Stevens 2001; Tsige, Lorenz et al. 2004). The polymers are treated as bead-spring molecules. The initial system is a mixture of two molecules. A two bead molecule represents the resin (Bisphenol A) which we label as molecule A. In this work, we introduce a more complicated crosslinker (molecule B) that models the T403 crosslinker as shown in Fig. 7-1, which has a central bead with three arms of length 2, 1 and 2 beads corresponding to the average lengths of each arm. The three terminal beads on the arms can each form two additional bonds with molecule A, which can form one additional bond for each of its beads. The number of cross-linkers in the system is determined by stoichiometry.

All beads interact through the standard Lennard-Jones (LJ) potential with a cutoff at 2.5*d* (Kremer and Grest 1995).

$$U_{LJ}(r) = 4u_0\left(\left(\frac{d}{r}\right)^{12} - \left(\frac{d}{r}\right)^{6}\right) \qquad (7\text{-}1)$$

where r is the separation distance, u_0 represents the LJ energy and d represents the size of a bead.

The masses of all the beads are taken to be equal, the time unit is τ and all quantities will be in LJ units. The traditional notation of σ and ε as the stress and strain, respectively, is used.

The geometry of the system starts with a stoichiometric liquid mixture of the two components between two rigid, solid surfaces. Each solid surface is composed of two fcc (111) layers perpendicular to the z-direction with a near neighbor spacing in the layer of $1.204d$. Periodic boundary conditions are imposed in the y-direction; the size of the simulation cell in this direction is $28d$ for all systems. The width in the x-direction w and the separation of the surfaces h varies with the system (see Table 7-1). The h/w ratio is about 10 in all cases so that the central region should not be influenced by the sides.

The polymeric system is composed initially of a stoichiometric mixture of the two molecules between two solid surfaces. The starting liquid extends to about $5d$ from the open ends of the surfaces. In the x-direction the system is open except during equilibration of the liquid mixture of the two components, when a wall potential is used to confine the liquid. After equilibration, the wall potential is removed and bonding to the surfaces and crosslinking of the liquid occurs as in previous simulations (Stevens 2001) . The crosslinking simulation time is long enough such that at least 95% of the possible bonds are formed. Crosslinking is performed slightly above the glass transition temperature. The systems is then cooled to $0.3u_0$ (below the glass transition temperature) and a simulation run until the thickness of the system reaches a steady state under a load ($0.1\ u_0/d^3$) on the top surface mimicking atmospheric pressure. To reach the steady state, the smallest system required a time of only 1000 τ, but larger systems required more; the largest system had a simulation time of 50000 τ. Tensile simulations are performed by pulling the top surface at a constant velocity of 0.001 d/τ. For system 2, the pull velocity was verified to be slow enough that there are not resolvable differences in the stress-strain curves compared to $10^{-4}\ d/\tau$.

7.3 Results

The stress-strain behavior is shown in Fig. 7-2 for the system sizes given in Table 7-1. The data has been boxcar smoothed. A clear dependence on h occurs in the stress-strain behavior at large strain, but the low strain behavior has similar behavior. The yield stress peak is identical for all systems. The yield stress is 2.85 u_0/d^3, and the yield strain ε_y is 0.073. For sufficiently large systems where the surfaces (including sides) are not affecting the bulk, the yield behavior should be independent of size, since the dynamics of the beads at small strains is local. For a wide range of $\varepsilon > \varepsilon_y$, the behavior is similar for all systems with the larger systems having smaller fluctuations. In this regime, there is a long plateau in the stress at about 2.2 u_0/d^3. From previous work (Stevens 2001; Stevens 2001), this plateau region is where the strands are being straightened by the tensile stress and very few of the bonds are being strained. Because the tensile pull is increasing the volume, voids are forming on the molecular scale (see Fig. 7-3). At larger ε, the stress rises because bonds are being stretched. At this point, a distinct size dependent behavior does occur. The rise in the stress is rather small in the largest systems remaining well below σ_y, while the smallest system has a maximum stress greater than σ_y. The failure strain ε_f is calculated as the strain value at which the stress is half the maximum. Clearly, the failure strain ε_f decreases as a function of system size.

The critical difference from the present work and past fracture simulations is the explicit treatment of the open sides and corners. The mode of fracture initiation is distinct due to the open boundary. Examination of images of the system as a function of strain show that in all systems, a crack forms in one (or two) of the corners as shown in Fig. 7-3 (see also Figs. 7-8 to 7-12 for images of the other systems simulated). The strain at which the crack appears ε_c is determined from visual inspection of the images of the dynamics. Fig. 7-4 shows the dependence on h of ε_c, ε_f and ε_p, the strain at the peak stress. Note that the ε_p are the same as ε_c given the uncertainty in both values, except for the smallest system. This equality is to be expected, since once the crack starts the stress also begins to be relieved and decreases.

The extrapolations in Fig. 7-4 have significant implications. For large h the extrapolation of ε_c implies cracks will form at zero strain for h near 550 d. (Simulations of larger h are not presently possible with our resources. The system 5 simulations already take about 2 months of CPU time.) This extrapolation comes from linear least squares fits to ε_f and ε_c. The extrapolation to $\varepsilon_f \to 0$ occurs near $h = 800d$. If we use $d = 1$ nm as an estimate of the bead size, then all these thicknesses are below a micron. These results imply that a major source of the difference between simulations of highly crosslinked polymer and experiments is the geometry and system size. The data suggests that the failure strains in simulations for larger system sizes could approach the strains typically seen in experiments (0.1-0.3). Directly comparing to experiments on adhesives on the submicron scale is limited by the sparse experimental data available on such thin systems due to inherent measurement challenges (Lau, Broderick et al. 2014).

An intriguing point is that this h-dependence implies the existence of a new length scale. The extrapolations of ε_c and ε_f are expected to break down, as new physical phenomena ought to occur as ε_c approaches ε_y let alone 0. Thus, there must be a thickness h^*, where the decreasing ε_c stops or changes. This h^* will be indicative a structural length scale that is significant in understanding large scale deformation in highly crosslinked polymer networks. Unfortunately, resolving this issue requires larger simulations than we can do.

In previous work on systems without open sides, we found the failure strain was correlated with the minimal paths in the network from bottom surface to the top surface, and this connection was the determining factor of the large failure strains (Stevens 2001). In the present systems, there is a difference in behavior between the sides and the center. In the center of the system, the behavior is similar to the early simulations, as the structure of the strands is similar to previous works. The minimal path lengths (i.e. the strain to make the minimal paths straight) in the center (written as a strain, $\varepsilon_{mp} \equiv P_{\min}/h - 1$) are in the range 1.30 to 1.33. The minimal paths near the edges are slightly shorter ($\varepsilon_{mp} \approx 1.26$), since the paths do not have complete freedom of direction that exists at the center, but this is not a source of the h dependence.

As Fig. 7-3 shows the shape of the sides changes with strain as the cohesive forces try to maintain the equilibrium density by contracting the polymer network from the sides, i.e., a reduction in the cross sectional area, which will be referred to as side contraction. The shape at the corners becomes an acute wedge that extends over a relatively long length as the side contract in. The minimal paths near the sides are stretched along a curved path, which is longer than the straight path for the central minimal paths. The paths near the sides are thus much more stretched at a given strain than paths in the center are. The minimal paths at the sides will become taut at lower strains than at the center because of the curved paths at the sides. The length of side as a function of ε was calculated (for a range of strains a parabola is a good fit to the shape). The dependence of the side shape and length as a function of strain has an interesting connection with ε_{mp} (see Fig. 7-5). For $\varepsilon < 0.55$ the amount of side contraction increases monotonically and is independent of the *h*. At larger ε the amount of side contraction decreases. This transition occurs when the side length approaches the minimal path length of the sides. Thus, at the sides there is a much larger strain than in the middle of the system and it saturates at ε_{mp}. Once the strain along the sides approaches close to the ε_{mp} the minimal paths along the side are almost taut and the degree of side contraction reverses to keep the side contour length constant. However, neither ε_f nor ε_c are correlated with this transition which is constant with respect to *h*.

In order to get a better understanding of the fracture dynamics, the location of individual bond breaking in the systems as a function of ε was examined. Bond breaking starts well below ε_c in two regions: in the voids and at the sides (see Fig. 7-6). Within the voids, the bond breaking is sporadic spatially and does not accumulate into a crack. However at the sides and particularly the corners, the number of broken bonds increases with strain and does result in cracks. As a function of *h*, the total number of broken bonds is monotonically increasing at $\varepsilon = 0.50$, which is below ε_c for all *h*. A concentration of bond breaking in the corners implies there is a concentration of stress there.

The local stress was calculated using the local virial with voronoi volumes (MacNeill and Rottler 2010). However, calculating the local stress encounters various limitations. The fluctuations in stress are large even when dealing with the whole system or surface. At the level of a smaller grid, the fluctuations will be even larger. We calculated the stress binned into bins of size $4d \times 4d$ in the *xz*-plane. At $\varepsilon = 0$, the stress is effectively uniform with no indication of high stress in the corners. However, as the strain increases, clear stress concentration in the corners is exhibited in σ_{xx} as shown in Fig. 7-7. Large values of σ_{zz} occur not in the corners but in the middle of the sides. These high stresses and their direction correlate with the deformed geometry and bond breaking discussed above. The contraction of the sides results in a wedge shaped geometry in the corners, with the bonds being primarily strained in the *x*-direction. Thus the corners have large σ_{xx}. The network at the middle of the sides is also strained by the tension, but at this location the strain is the *z*-direction. Thus the middle of the sides have large σ_{zz}. We note that within the system the nanovoiding also give pockets of large σ_{zz} in the interior.

These tensile simulations of a coarse-grained highly crosslinked polymer system with open sides have produced several important results. The failure stain decreases substantially as the system size is increased, showing that system size and boundary conditions are critical. Extrapolating this size effect implies that systems with thickness of less than a micron will have failure strains similar to observed in experiments. Thus, a major source of the large difference in failure strains between simulation and experiment has been identified. Moreover, the results imply the existence of a crossover, where the failure strain stops decreasing with system size, and this crossover corresponds to an important length scale in the polymer adhesive system that has not be characterized. As in experiments the open sides result in the stresses that cause bond breaking to localize predominantly in the corners. Crack initiation is found to occur in the corners as would be expected from linear elastic fracture mechanics, although with such large strains the system is not in the linear regime. Future simulations will address larger systems to observe the transition in $\varepsilon_f(h)$ and to determine the structural feature(s) that determine the transition.

Table 7-1 Systems in MD simulations

index	*N*	*h*	*w*
1	513600	40.4	417.1
2	1975200	76.1	834.2
3	7747200	149.0	1668.3
4	17316000	222.3	2502.5
5	30681600	295.0	3366.6

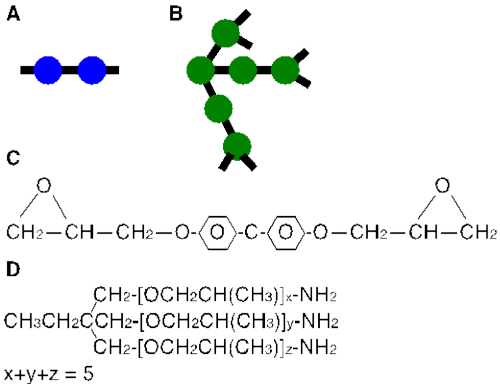

Figure 7-1. Schematic of the molecular components of the model epoxy. Molecule A is the coarse-grained representation of Bisphenol A (molecule C). Molecule B is the coarse-grained representation of the T403 crosslinker (molecule D). The terminal beads have two open bonds on the T403 representing the NH_2 terminal group.

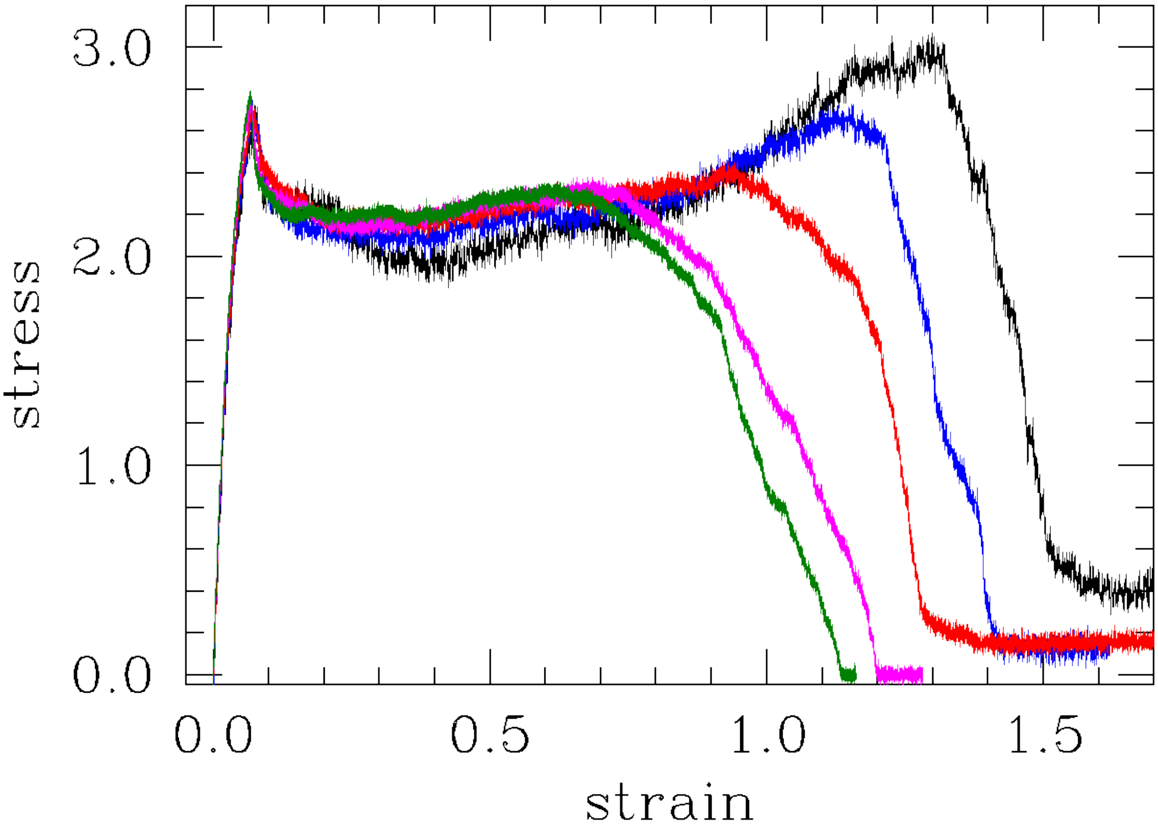

Figure 7-2. The stress-strain curves as a function of system size for systems 1-5. Colors are black, blue, red, magenta and green for systems 1 to 5, respectively.

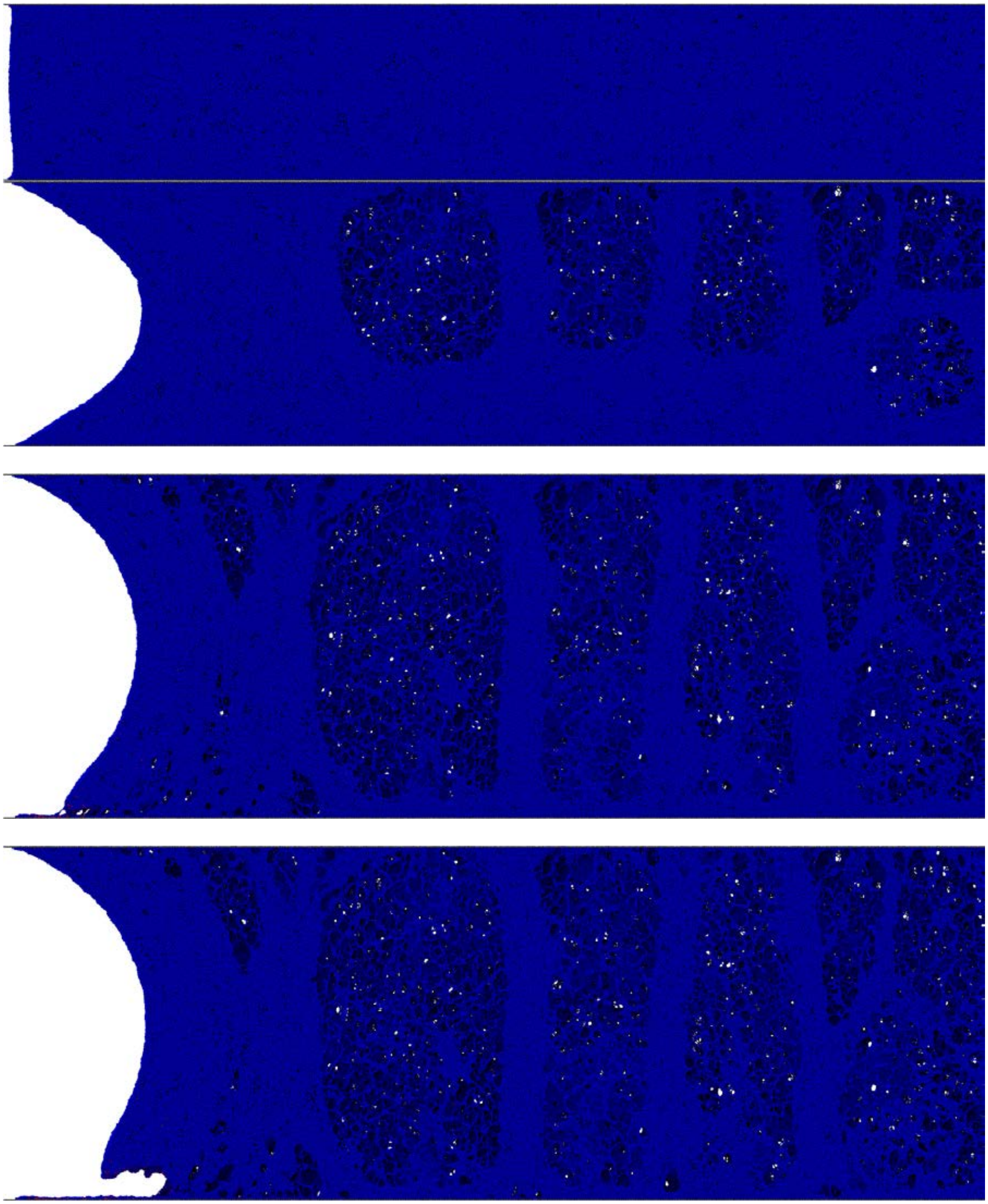

Figure 7-3 Images of left half of system 3 at various ε showing crack formation at corner and contraction of side. Void formation is also visible for ε > 0. From top to bottom ε = 0, 0.50, 0.95 and 1.00.

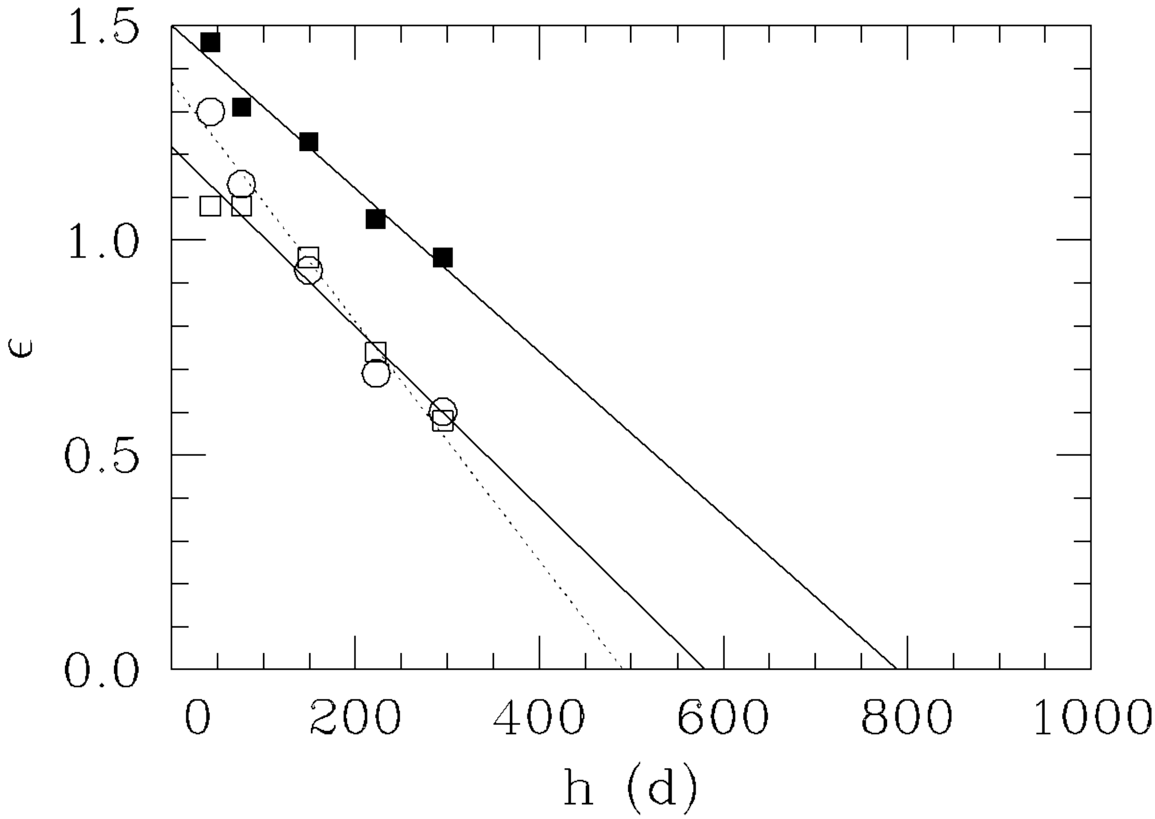

Figure 7-4. The failure (solid squares), (second) maximum peak stress (open circles) and crack initiation (open squares) strains as a function of the adhesive thickness (*h*).The lines are separate least squares fits to each data set, with the dotted line for the ε_p data and the solid lines for the other two.

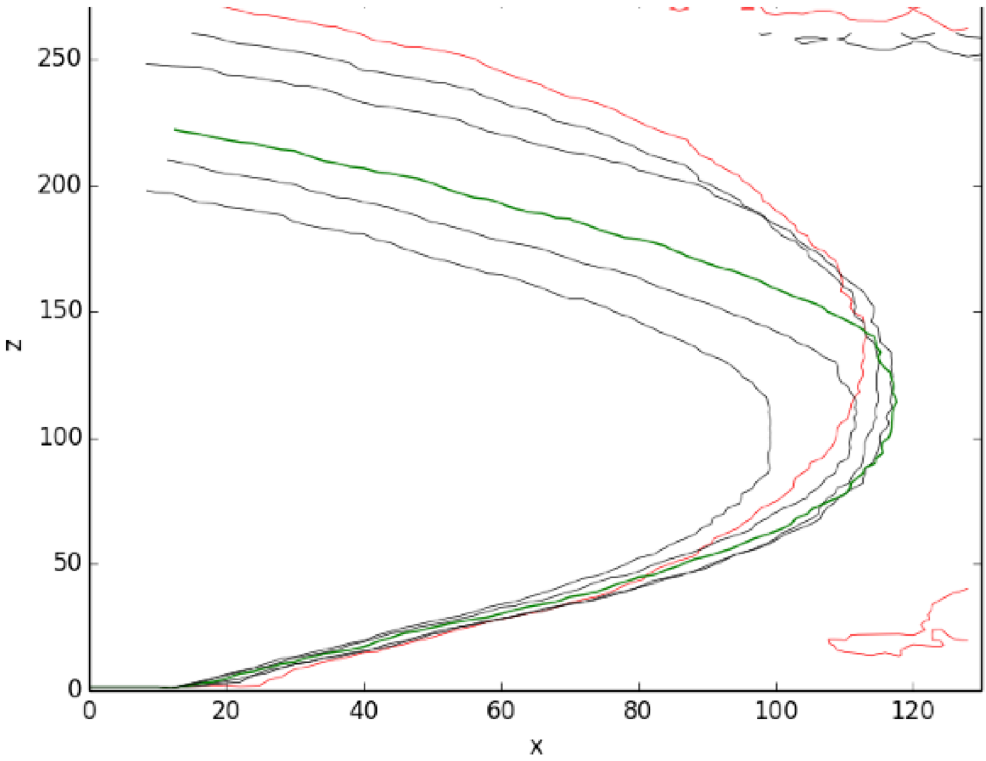

Figure 7-5. Strain dependence of the left side for system 3. ε = 0.33, 0.415, 0.50, 0.60 (green), 0.75 and 0.83 (red). Some contours away from the side show up at the two largest strains due to void formation at these large strains.

The main features are that the inward extent increases with strain to about ε = 0.60, which is shown in green. By this strain, the length of the side has reached the minimal path length of the network at the sides. At larger strains, the inward extent *decreases* so that the total side length remains about constant. For system 3 this behavior continues to much larger strains before a crack forms in the corner.

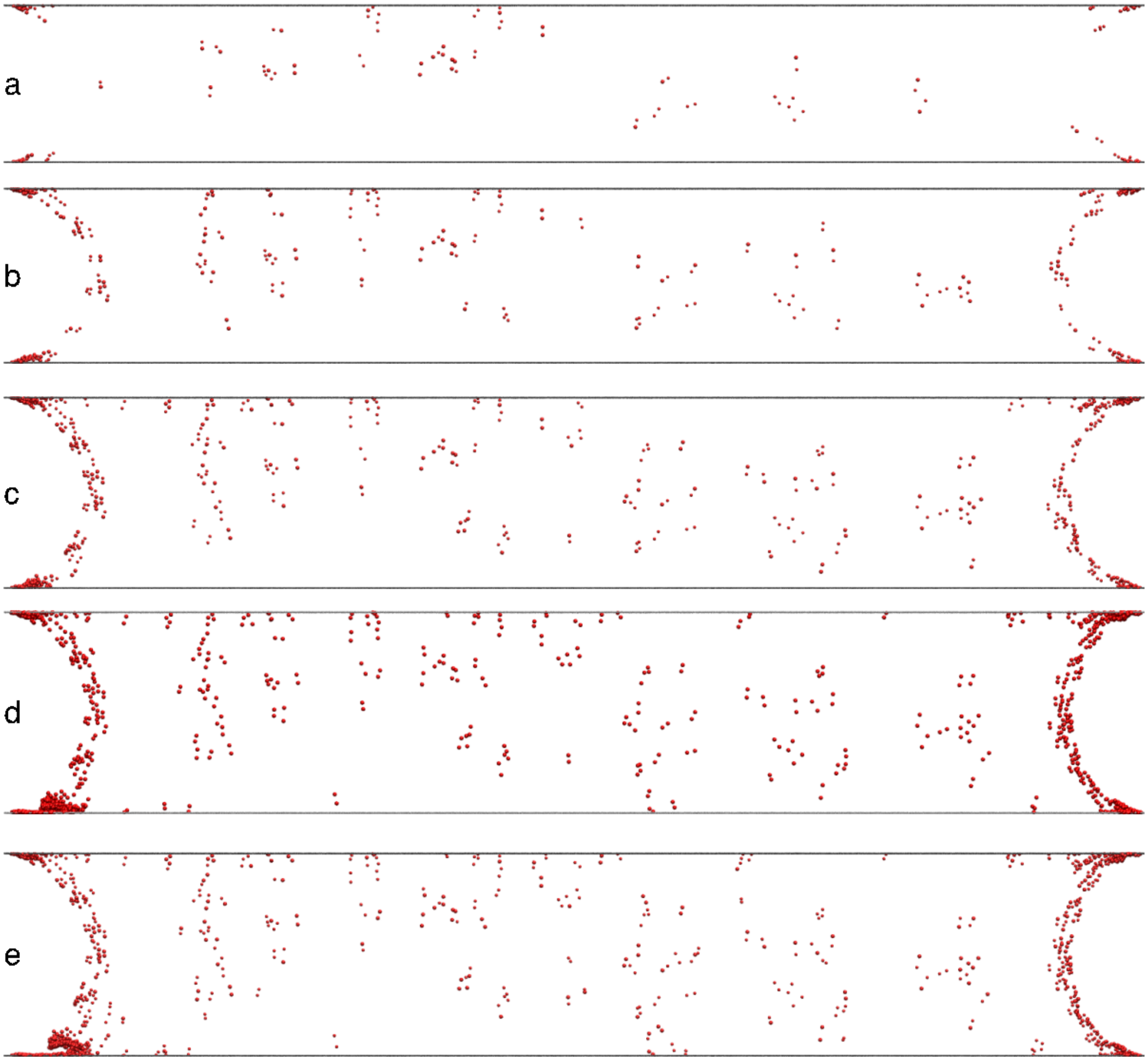

Figure 7-6. Images showing broken bonds (red) and surfaces (gray) as a function of strain for system 3. ε = a) 0.50 b) 0.67 c) 0.83 d) 0.95 e) 1.00.

Bond breaking does start well before ε_c, but initially it is mostly isolated bonds. An accumulation of bond breaking in the corners and along the sides occurs as the strain approaches ε_c, and finally a crack forms once sufficient bond breaking in the corner occurs.

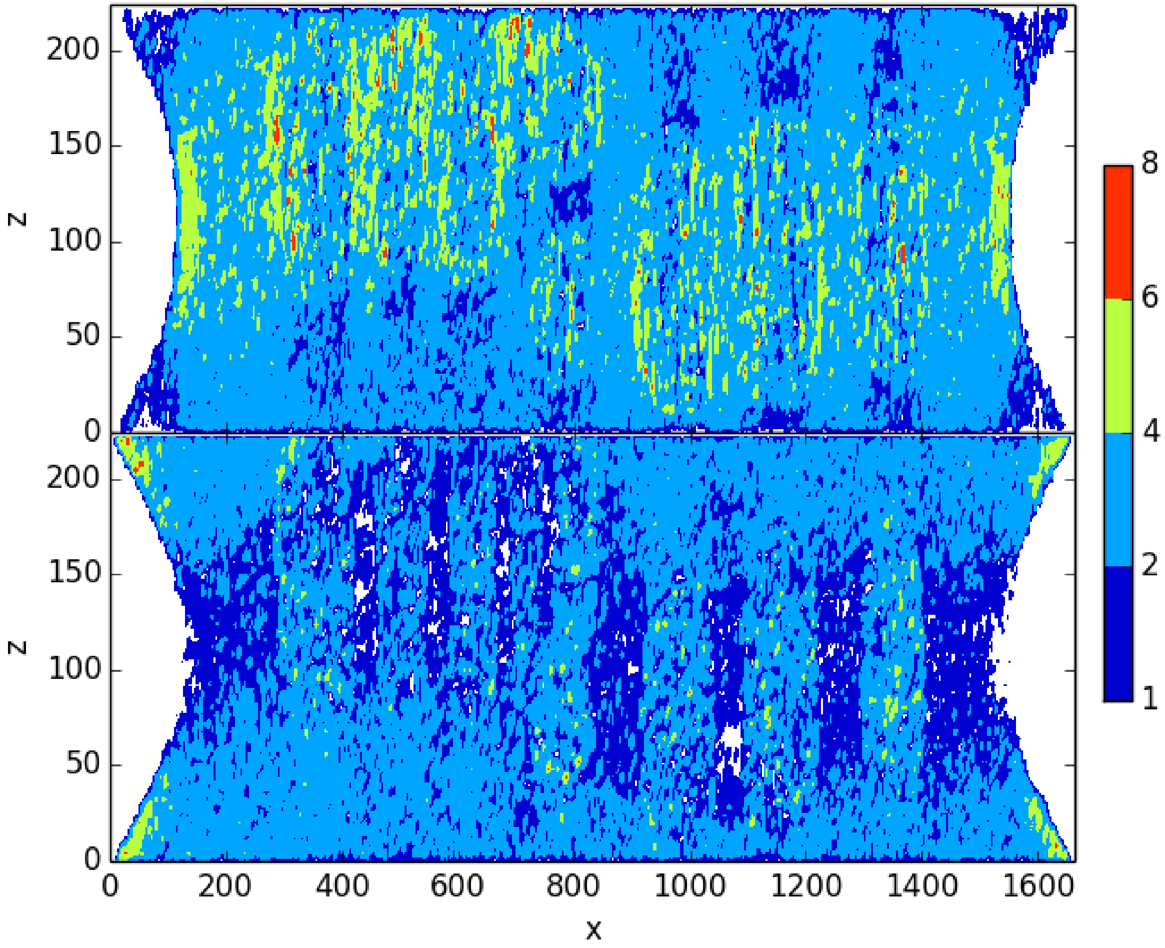

Figure 7-7. The local stresses σ_{zz} (top) and σ_{xx} (bottom) for system 3 at $\varepsilon = 0.50$.

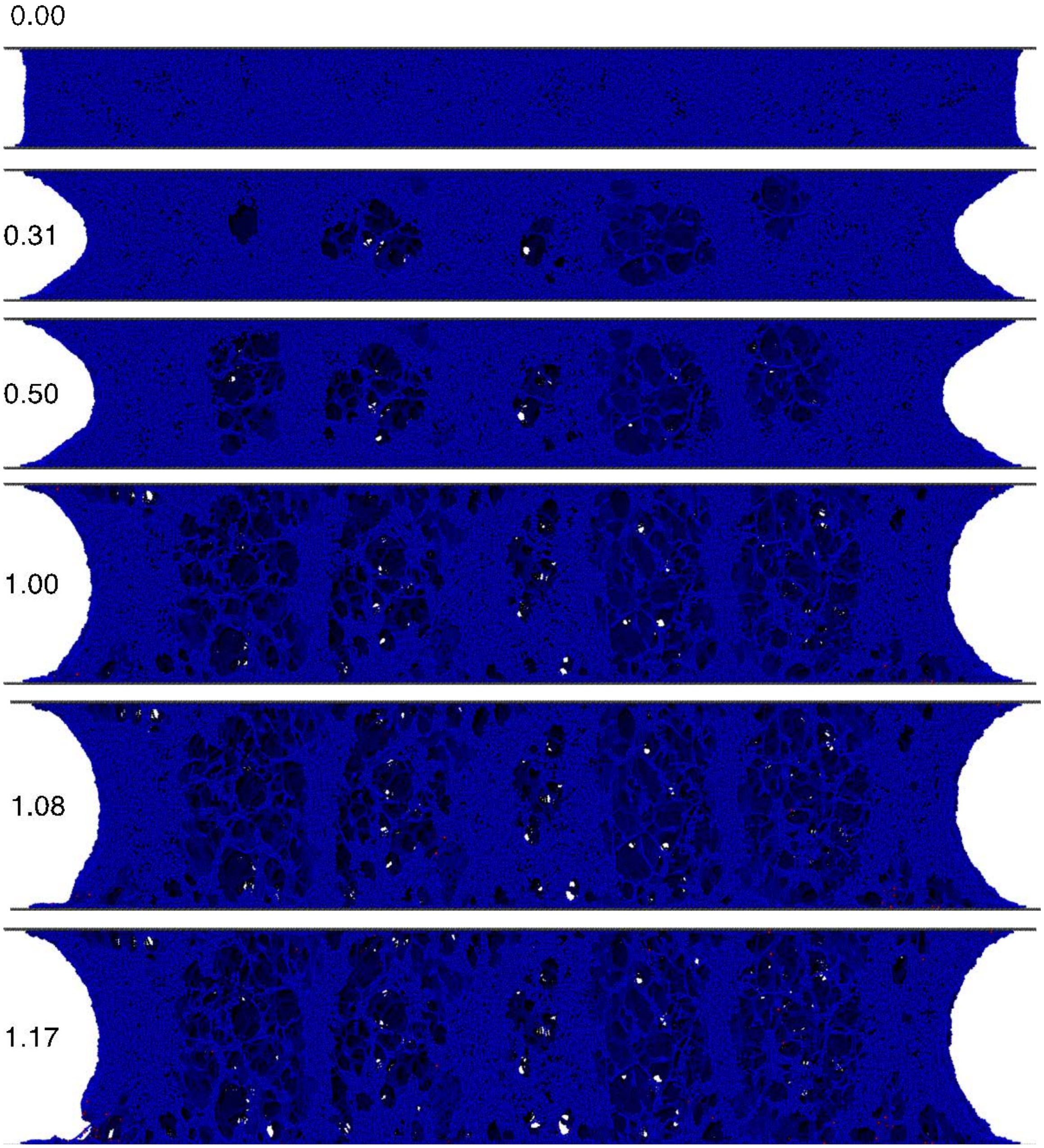

Figure 7-8. Images of system 1 at various ε showing crack formation at corner and contraction of side.

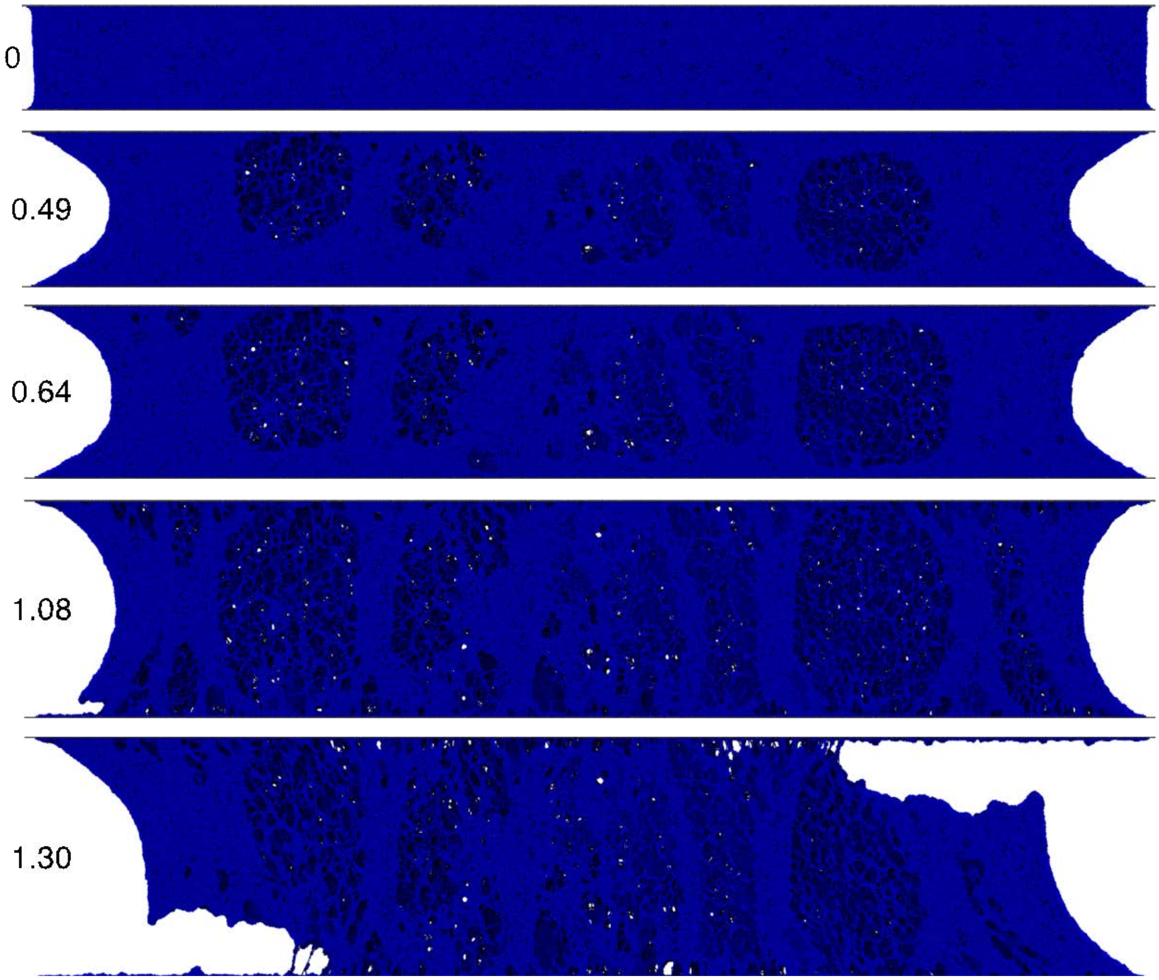

Figure 7-9. Images of system 2 at various ε showing crack formation at corner and contraction of side.

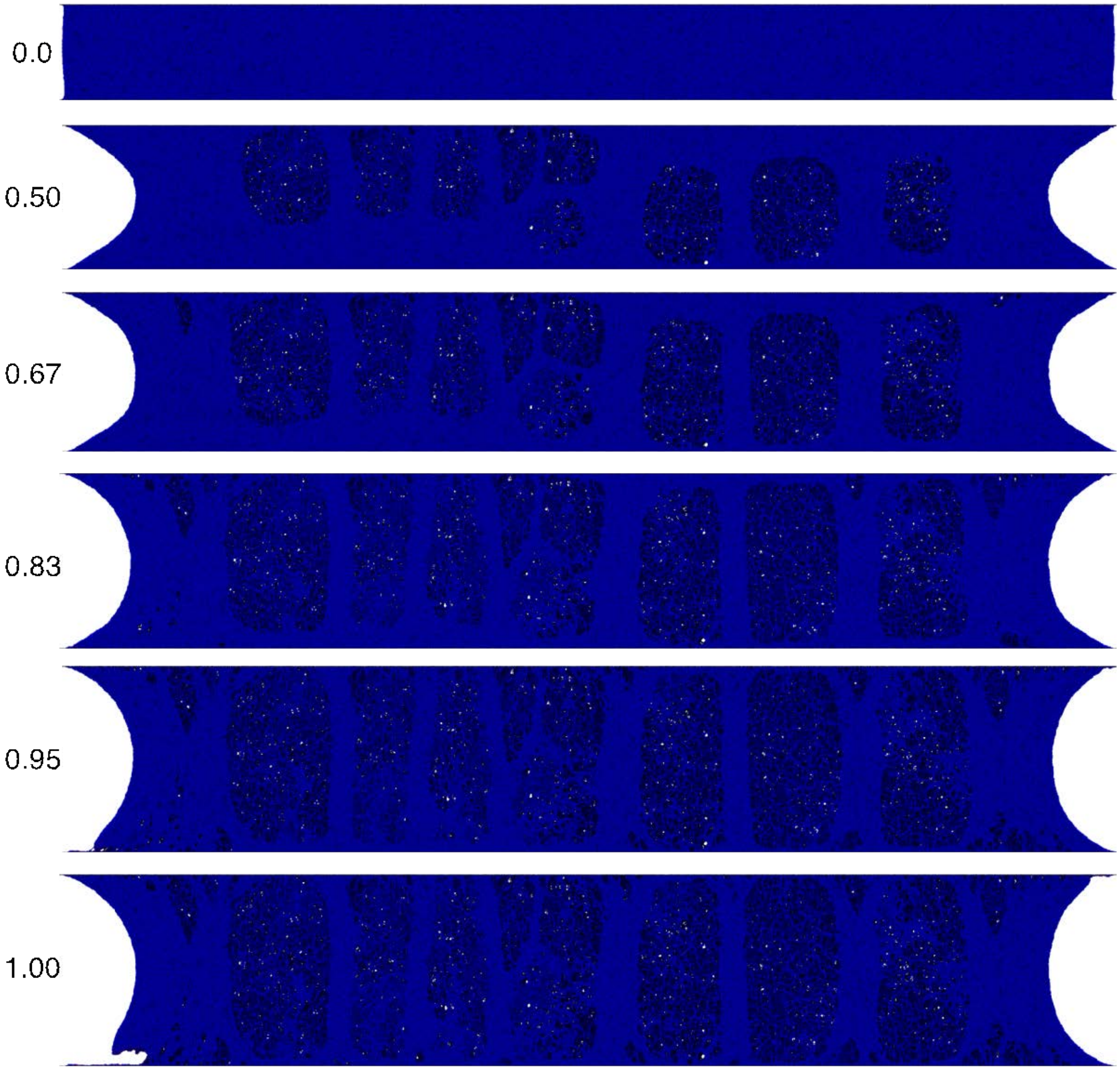

Figure 7-10. Images of system 3 at various ε showing crack formation at corner and contraction of side.

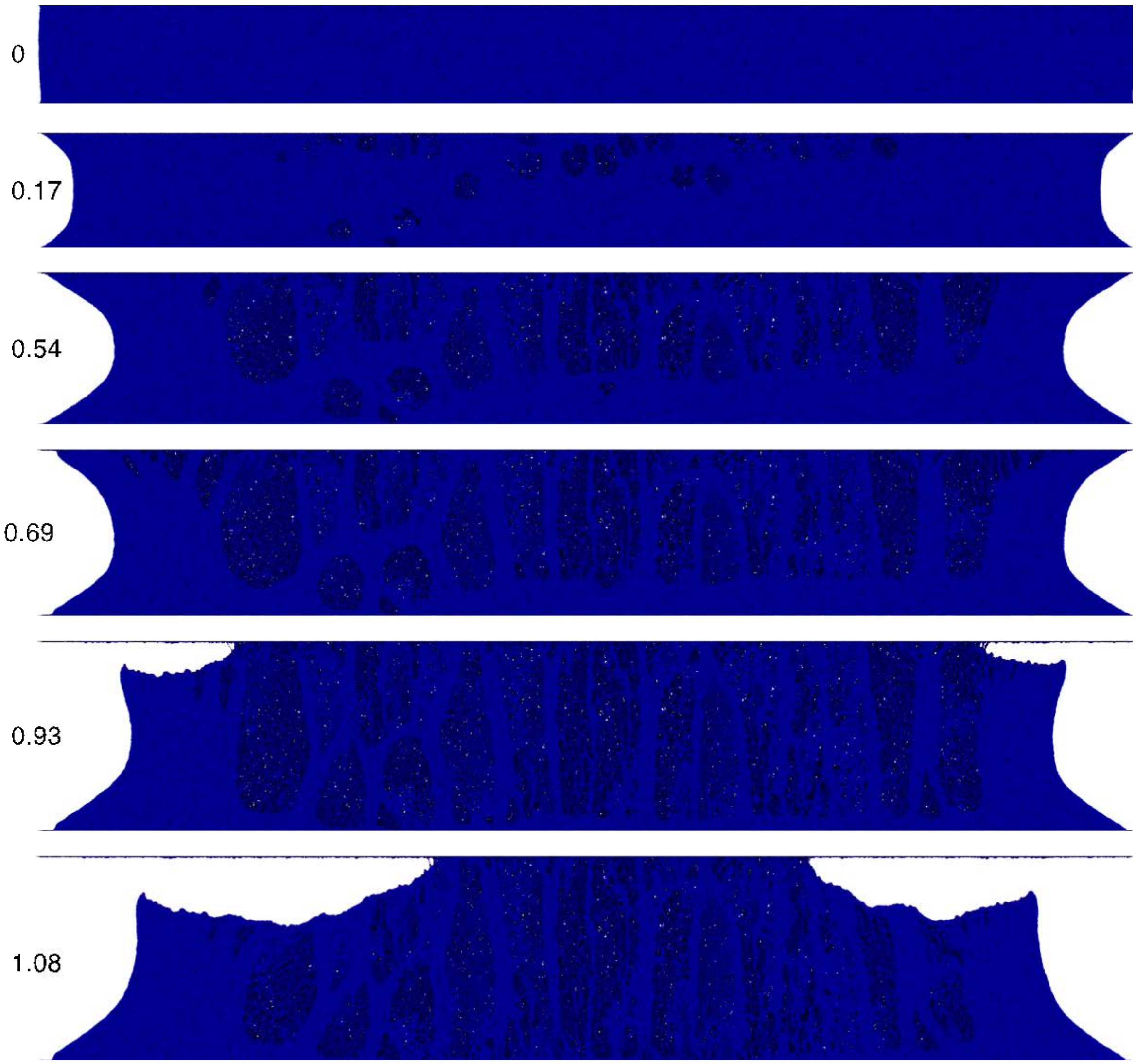

Figure 7-11. Images of system 4 at various ε showing crack formation at corner and contraction of side.

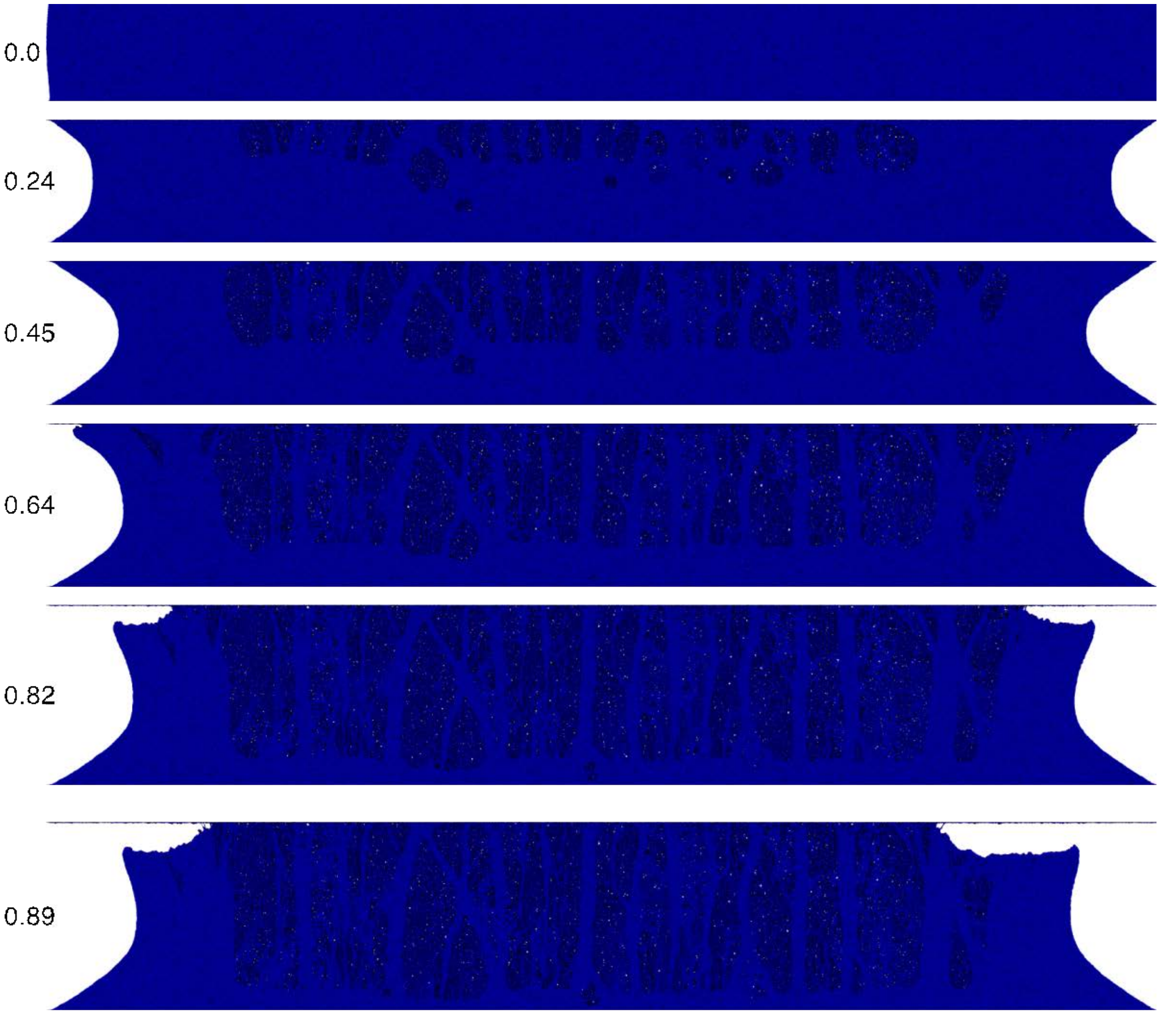

Figure 7-12. Images of system 5 at various ε showing crack formation at corner and contraction of side.

8. SUMMARY OF MAJOR ACCOMPLISHMENTS, PUBLICATIONS, AND PRESENTATIONS

8.1 Accomplishments

1) Developed a new type of cohesive zone model (the MDG$_c$ CZM) that directly incorporates the controlling feature of interfacial fracture: a rapid increase in toughness with increasing interfacial shear (Reedy and Emery 2014). Implemented the MDG$_c$ CZ model in Sierra/SolidMechanics.

2) To our knowledge, were first to quantify the increase in interfacial toughness with decreasing temperature (85% increase at -65C). This helps to explain paradox of why joint strength increases when decreasing temperature.

3) Developed a new coarse-grained model for highly crosslinked polymer networks to more accurately represent molecular packing at the interface and bond failure. The simulations showed a strong dependence on system size.

8.2 Journal publications

1. Reedy, E.D., Jr. and Emery, J.M., A Simple Cohesive Zone Model that Generates a Mode-mixity Dependent Toughness. International Journal of Solids and Structures, 2014. 51: p. 3727-3734.
2. Reedy, E.D., Jr., Cohesive Zone Finite Element Analysis of Crack Initiation from a Butt Joint's Interface Corner. International Journal of Solids and Structures, 2014. 51: p. 4336-4344.
3. Stevens, M.J., Role of Corners in Fracture of Polymeric Adhesives. Submitted for publication.

8.3 Conference proceedings

1. Reedy, E.D., Jr. and Emery, J.M., A Simple Mode-mixity Dependent Cohesive Zone Model with Application to Illustrative Interfacial Fracture Problems, in Proceedings of the 37th Annual Meeting of The Adhesion Society, San Diego, CA, 2014.
2. Reedy, E.D., Jr., A Simple, Mixed-Mode Dependent Cohesive Zone Model, in Proceedings of the 38th Annual Meeting of The Adhesion Society, Savannah, GA, 2015.
3. Kropka, J.M, Spangler, S.W., Stavig, M.E., and Chambers, R.S., Residual Stress Developed During the Cure of Thermosetting Polymers, in Proceedings of the 38th Annual Meeting of The Adhesion Society, Savannah, GA, 2015.
4. Stevens, M., Molecular Dynamics Simulation of Fracture Initiation at a Corner, in Proceedings of the 38th Annual Meeting of The Adhesion Society, Savannah, GA, 2015.

8.4 Posters

1. Clarkson, C.M., McCoy, J.D., Chambers, R.S.and Kropka, J.M., Measurement and Modeling of the Effect of Aging on the Compressive Yield of Epoxy, American Physical Society March Meeting, Denver, CO, 2014.
2. Arechederra, G.K., Reprogle, R.C, Clarkson, C.M., McCoy, J.D., Kropka, J.M., Long, K.N., and Chambers, R.S., Strain Rate Dependence of Compressive Yield and Relaxation in DGEBA Epoxies, American Physical Society March Meeting, San Antonio, TX, 2015.
3. Clarkson, C.M., McCoy, J.D., and Kropka, J.M., Enthalpy Relaxation of a DGEBA Epoxy as a function of Time, Temperature, and Cooling Rate, American Physical Society March Meeting, San Antonio, TX, 2015.

9. REFERENCES

Adolf, D. B., R. S. Chambers and J. M. Caruthers (2004). "Extensive validation of a thermodynamically consistent, nonlinear viscoelastic model for glassy polymers." Polymer **45**(13): 4599-4621.

Adolf, D. B., R. S. Chambers and M. A. Neidigk (2009). "A simplified potential energy clock model for glassy polymers." Polymer **50**(17): 4257-4269.

Bao, G., S. Ho, Z. Suo and B. Fan (1992). "The Role of Material Orthotropy in Fracture Specimens for Composites." International Journal of Solids and Structures **29**: 1105-1116.

Barenblatt, G. I. (1962). The Mathematical Theory of Equilibrium Cracks in Brittle Fracture. Advances in Applied Mechanics. H. L. Dryden and T. von Kármán, Elsevier. **Volume 7:** 55-129.

Cao, H. C. and A. G. Evans (1989). "An Experimental Study of the Fracture Resistance of Bimaterial Interfaces." Mechanics of Materials **7**: 295-304.

Caruthers, J. M., D. B. Adolf, R. S. Chambers and P. Shrikhande (2004). "A thermodynamically consistent, nonlinear viscoelastic approach for modeling glassy polymers." Polymer **45**(13): 4577-4597.

Chen, W. and B. Zhou (1998). "Consitutive behavior of Epon 828/T-403 at various strain rates." Mechanics of Time-Dependent Materials **2**: 103-111.

Chikina, I. and C. Gay (2000). "Cavitation in Adhesives." Phys. Rev. Lett. **85**: 4546--4549.

Cordill, M. J., D. F. Bahr, N. R. Moody and W. W. Gerberich (2007). "Adhesion measurements using telephone cord buckles." Materials Science and Engineering a-Structural Materials Properties Microstructure and Processing **443**(1-2): 150-155.

Dundurs, J. (1969). "Discussion of edge-bonded dissimilar orthogonal elastic wedges under normal and shear loading." Journal of Applied Mechanics **36**: 650-652.

Gay, C. and L. Leibler (1999). "Theory of Tackiness." Phys. Rev. Lett. **82**: 936--939.

Guan, P., S. Lu, M. J. B. Spector, P. K. Valavala and M. L. Falk (2013). "Cavitation in Amorphous Solids." Phys. Rev. Lett. **110**: 185502.

Hutchinson, J. W. and Z. Suo (1992). Mixed mode cracking in layered materials. Advances in Applied Mechanics. J. W. Hutchinson and T. Y. Wu, Academic Press. **29:** 63-191.

Kendall, K. (1994). "Adhesion: Molecules and Mechanics." Science **263**: 1720-1725.

Kinloch, A. J. (1987). Adhesion and Adhesives. New York, Chapman and Hall.

Kremer, K. and G. S. Grest (1995). Entanglement effects in Polymer Melts and Networks. Monte Carlo and Molecular Dynamics Simulations in Polymer Science. K. Binder. New York, Oxford**:** 194-271.

Lau, D., K. Broderick, M. J. Buehler and O. Büyüköztürk (2014). "A robust nanoscale experimental quantification of fracture energy in a bilayer material system." Proceedings of the National Academy of Sciences **111**: 11990-11995.

Leaderman, H. (1943). Elastic and Creep Properties of Filamentous Materials and other high polymers. Washington, The Textile Foundation.

Li, C., G. A. Medvedev, E. Lee, J. Kim, J. M. Caruthers and A. Strachan (2012). "Molecular dynamics simulations and experimental studies of the thermomechanical response of an epoxy thermoset polymer." Polymer **53**: 4222-4230.

Li, C. and A. Strachan (2015). "Coarse-grained molecular dynamics simulations of the tensile behavior of a thermosetting polymer." J. Polymer Science, B **53**: 103-122.

Liechti, K. M. and Y. S. Chai (1992). "Asymmetric Shielding in Interfacial Fracture Under In-Plane Shear." Journal of Applied Mechanics **59**: 295-304.

Liu, H., M. Li, Z. Lu, Z. Zhang, C. Sun and T. Cui (2011). "Multiscale Simulation Study on the Curing Reaction and the Network Structure in a Typical Epoxy System." Macromolecules **44**: 8650--8660.

MacNeill, D. and J. Rottler (2010). "From macroscopic yield criteria to atomic stresses in polymer glasses." Phys. Rev. E **81**: 011804.

Makke, A., M. Perez, J. Rottler, O. Lame and J.-L. Barrat (2011). "Predictors of cavitation in glassy polymers under tensile strain: a coarse-grained molecular dynamics investigation." Macromolecular Theory and Simulations **20**: 826-836.

Matos, P. P. L., R. M. McMeeking, P. G. Charalambides and M. D. Drory (1989). "A method for calculating stress intensities in bimaterial fracture." International Journal of Fracture **40**: 235-254.

Mello, A. W. and K. M. Liechti (2006). "The effect of self-assembled monolayers on interfacial fracture." Journal of Applied Mechanics-Transactions of the ASME **73**(5): 860-870.

Morgan, R. J., F.-M. Kong and C. M. Walkup (1984). "Structure-property relations of polyethertriamine-cured bisphenol-A-diglycidyl ether epoxies." Polymer **25**: 375 - 386.

Needleman, A. (1987). "A continuum model for void nucleation by inclusion debonding." Journal of Applied Mechanics **54**(3): 525-531.

Park, K. and G. H. Paulino (2011). "Cohesive Zone Models: A Critical Review of Traction-Separation Relationships Across Fracture Surfaces." Applied Mechanics Reviews **64**(6).

Reedy, E. D., Jr. (1990). "Intensity of the Stress Singularity at the Interface Corner Between a Bonded Elastic and Rigid Layer." Engineering Fracture Mechanics **36**: 575-583.

Reedy, E. D., Jr. (1993). "Asymptotic Interface Corner Solutions for Butt Tensile Joints." International Journal of Solids and Structures **30**: 767-777.

Reedy, E. D., Jr. (2014). "Cohesive Zone Finite Element Analysis of Crack Initiation from a Butt Joint’s Interface Corner." International Journal of Solids and Structures **51**: 4336-4344.

Reedy, E. D., Jr. and J. M. Emery (2014). "A Simple Cohesive Zone Model that Generates a Mode-mixity Dependent Toughness." International Journal of Solids and Structures **51**: 3727-3734.

Reedy, E. D., Jr. and T. R. Guess (1999). "Additional Interface Corner Toughness Data for an Adhesively-Bonded Butt Joint." International Journal of Fracture **98**: L3-L8.

Rice, J. R. (1988). "Elastic fracture mechanics concepts for interfacial cracks." Journal of Applied Mechanics **55**: 98-103.

Rottler, J. (2009). "Fracture in glassy polymers: a molecular modeling perspective." J.Physics: Condensed Matter **21**: 463101.

Schwarzl, F. and A. J. Staverman (1952). "TIME-TEMPERATURE DEPENDENCE OF LINEAR VISCOELASTIC BEHAVIOR." Journal of Applied Physics **23**(8): 838-843.

Stevens, M. J. (2001). "Interfacial fracture between highly cross-linked polymer networks and a solid surface: Effect of interfacial bond density." Macromolecules **34**(8): 2710-2718.

Stevens, M. J. (2001). "Manipulating connectivity to control fracture in network polymer adhesives." Macromolecules **34**(5): 1411-1415.

Suo, Z. and J. W. Hutchinson (1989). "Sandwich Test Specimens for Measuring Interface Crack Toughness." Materials Science and Engineering **A107**: 135-143.

Swadener, J. G. and K. M. Liechti (1998). "Asymmetric Shielding Mechanisms in the Mixed-Mode Fracture of a Glass/Epoxy Interface." Journal of Applied Mechanics **65**: 25-29.

Thomas, J. D. (2011). Sierra/SolidMechanics 4.22 User’s Guide, SAND2011-7597. SIERRA Solid Mechanics Team Albuquerque, Sandia National Laboratories.

Timoshenko, S. P. and J. N. Goodier (1970). New York, McGraw-Hill Book Company.

Tsige, M., C. D. Lorenz and M. J. Stevens (2004). "Role of Network Connectivity on the Mechanical Properties of Highly Cross-Linked Polymers." Macromolecules **37**: 8466-8472.

Tvergaard, V. and J. W. Hutchinson (1992). "The relation between crack growth resistance and fracture process parameters in elastic -plastic solids." Journal of the Mechanics and Physics of Solids **40**(6): 1377-1397.

Tvergaard, V. and J. W. Hutchinson (1993). "The influence of plasticity on mixed mode interface toughness." Journal of the Mechanics and Physics of Solids **41**: 1119-1135.

Vafek, O. and M. O. Robbins (1999). "Molecular Dynamics Study of the Stress Singularity at a Corner." Physical Review B **60**: 12002-12006.

Varshney, V., S. S. Patnaik, A. K. Roy and B. L. Farmer (2008). "A Molecular Dynamics Study of Epoxy-Based Networks: Cross-Linking Procedure and Prediction of Molecular and Material Properties." Macromolecules **41**: 6837-6842.

Wang, J. S. and Z. Suo (1990). "Experimental determination of interfacial toughness curves using Brazil-nut-sandwiches." Acta Metallurgica et Materialia **38**(7): 1279-1290.

Williams, M. (1952). "Stress singularities resulting from various boundary conditions in angular corners of plates in extension." Journal of Applied Mechanics **19**: 526-528.

Williams, M. L., R. F. Landel and J D. Ferry (1955). "THE TEMPERATURE DEPENDENCE OF RELAXATION MECHANISMS IN AMORPHOUS POLYMERS AND OTHER GLASS-FORMING LIQUIDS." Journal of the American Chemical Society **77**(14): 3701-3707.

Wu, C. and W. Xu (2006). "Atomistic molecular modelling of crosslinked epoxy resin." Polymer **47**(16): 6004 - 6009.

Wu, C. and W. Xu (2007). "Atomistic molecular simulations of structure and dynamics of crosslinked epoxy resin." Polymer **48(**19): 5802 - 5812.

Yang, Q. D. and M. D. Thouless (2001). "Mixed-mode fracture analyses of plastically-deforming adhesive joints." International Journal of Fracture **110**(2): 175-187.

Yang, S., F. Gao and J. Qu (2013). "A molecular dynamics study of tensile strength between a highly-crosslinked epoxy molding compound and a copper substrate." Polymer **54**: 5064 - 5074.

Yang, S. and J. Qu (2014). "Coarse-grained molecular dynamics simulations of the tensile behavior of a thermosetting polymer." Phys. Rev. E **90**: 012601.

Yoshimoto, K., T. S. Jain, K. V. Workum, P. F. Nealey and J. J. de Pablo (2004). "Mechanical Heterogeneities in Model Polymer Glasses at Small Length Scales." Phys. Rev. Lett. **93**: 175501.

DISTRIBUTION

1	MS0346	M. R. Ford	1526
1	MS0346	R. D. Jamison	1526
1	MS0346	M. K. Neilsen	1526
1	MS0346	D. E. Peebles	1526
1	MS0840	J. E. Bishop	1554
1	MS0840	J. Cox	1554
1	MS0840	J. M. Emery	1526
1	MS0840	H. E. Fang	1554
1	MS0840	K. N. Long	1554
1	MS0878	A. K. Kaczmarowski	2735
1	MS0878	R. A. Roach	2735
1	MS0888	J. R. McElhanon	1853
1	MS0889	J. Carroll	1851
1	MS0889	S. J. Grutzik	1851
1	MS0889	H. Sumali	1851
1	MS0889	E. D. Reedy	1526
1	MS0958	L. G. Hughes	1853
1	MS0958	J. M. Kropka	1853
1	MS0958	M. E. Stavig	1853
1	MS1315	M. J. Stevens	1814
1	MS1411	A. C. Sun	1814
1	MS0899	Technical Library	9536
1	MS0359	D. Chavez, LDRD Office	1911

Sandia National Laboratories